

Anomalous-Hall Néel textures in altermagnetic materials

Rui-Chun Xiao,^{1,2,*} Hui Li,^{1,2} Hui Han,^{1,2} Wei Gan,¹ Mengmeng Yang,^{1,2} Ding-Fu Shao,³ Shu-Hui Zhang,⁴ Yang Gao,⁵ Mingliang Tian,^{6,7,†} Jianhui Zhou^{6,‡}

¹*Institute of Physical Science and Information Technology, Anhui University, Hefei 230601, China*

²*Anhui Provincial Key Laboratory of Magnetic Functional Materials and Devices, School of Materials Science and Engineering, Anhui University, Hefei 230601, China*

³*Key Laboratory of Materials Physics, Institute of Solid State Physics, Chinese Academy of Sciences, 230031 Hefei, China*

⁴*College of Mathematics and Physics, Beijing University of Chemical Technology, Beijing 100029, China*

⁵*Department of Physics, University of Science and Technology of China, Hefei 230026, China.*

⁶*Anhui Key Laboratory of Low-Energy Quantum Materials and Devices, High Magnetic Field Laboratory, HFIPS, Anhui, Chinese Academy of Sciences, Hefei, Anhui 230031, China.*

⁷*School of Physics and Optoelectronics Engineering, Anhui University, Hefei 230601, China*

*xiaoruichun@ahu.edu.cn; †mltian@ahu.edu.cn; ‡jhzhou@hmfll.ac.cn

Recently, the altermagnets, a new kind of colinear antiferromagnet with zero net magnetization and momentum-dependent spin-splitting of bands, have sparked great interest. Despite simple magnetic structures, these altermagnets exhibit intriguing and intricate dependence of AHE on the Néel vector, in contrast to the conventional perpendicular configuration of Hall current with magnetization in ferromagnets. In spite of being a crucial aspect in AHE research, the relationship between the AHE and the Néel vector remains largely elusive. Here, we propose a powerful "extrinsic parameter" method and further reveal diverse unconventional anomalous Hall textures in the Néel vector space, dubbed anomalous-Hall Néel textures (AHNTs) for altermagnets. Notably, we find that AHNTs resemble the spin textures in momentum space, and further reveal their symmetry origin. We identify 10 types across four categories of AHNTs in altermagnets. Meanwhile, we examine our key discoveries in prototypical altermagnets. Our work offers a complete classification of AHNTs and a thorough understanding of AHE in altermagnets.

Introduction. The anomalous Hall effect (AHE) [1] and its optical counterpart magneto-optical effect (Kerr and Faraday effect) [2] are the salient manifestations of time-reversal symmetry breaking in magnetically ordered materials. The Hall current $\mathbf{j}_H = \boldsymbol{\sigma}_H \times \mathbf{E}$ is determined by anomalous Hall vector, $\boldsymbol{\sigma}_H = (\sigma_x, \sigma_y, \sigma_z)$, and $\sigma_i = \varepsilon_{ijk} \sigma_{jk}^A$ ($i, j, k \in (x, y, z)$) is the anomalous Hall conductivity which is intimately linked to the Berry curvature of electrons in momentum space [3,4]. In ferromagnets and ferrimagnets, $\boldsymbol{\sigma}_H$ is usually believed to be parallel to the magnetization \mathbf{M} , that is, the radial structure ($\boldsymbol{\sigma}_H \parallel \mathbf{M}$) in the magnetization space (such as Fig. 1(a)), which leads to the conventional perpendicular configuration $\mathbf{j}_H \perp \mathbf{M}$. This long-time belief has been revisited by the recent progress of in-plane AHE [5-9]. Notably, AHE has been observed in fully compensated antiferromagnetic (AFM) materials [4,10-12]. Moreover, in these systems, the radial components $\boldsymbol{\sigma}_H \parallel \mathbf{M}$ in the different spin sublattices are canceled; however, the non-radial components may exist and exhibit complicated AHE behaviors.

Altermagnets [13-19], classified within the realm of collinear AFM materials, feature vanishing net magnetization constrained by symmetry, but exhibit momentum-dependent spin-split band structures akin to ferromagnets [20-25].

Remarkably, AHE [26-36] and the magneto-optical effects [37,38] have been observed in these materials, inspiring intensive investigations [39-45]. Despite the relatively simple magnetic structures in altermagnetic materials, the relationship between $\boldsymbol{\sigma}_H$ and the Néel vector \mathbf{n} (the unit vector indicating the magnetic direction difference between two spin sublattices) unexpectedly exhibits rich and some puzzling features [32,37,46,47], unlike the conventional radial structure ($\boldsymbol{\sigma}_H \parallel \mathbf{M}$) in ferromagnets. Despite of several case-by-case studies in specific altermagnets on AHE, a proper theory to derive the analytical and complete expression of $\boldsymbol{\sigma}_H$ in the Néel vector space for all altermagnets remains elusive.

In this work, we develop an "extrinsic parameter" method and corresponding computational algorithm to investigate anomalous Hall configurations in the Néel vector space $\boldsymbol{\sigma}_H(\mathbf{n})$ for altermagnets, which can be dubbed as anomalous-Hall Néel textures (AHNTs). We further establish a complete classification of these AHNTs, and find AHNTs exhibit unusual relationships in analogy to the spin textures [48-50] in momentum space (Fig. 1), such as Dresselhaus-like, Rashba-like, persistent, and pure cubic textures. Furthermore, we classify the altermagnetic materials according to the types of AHNTs and further verify our main results in rutile-type, calcite-type, NiAs-type, and perovskite-type altermagnets.

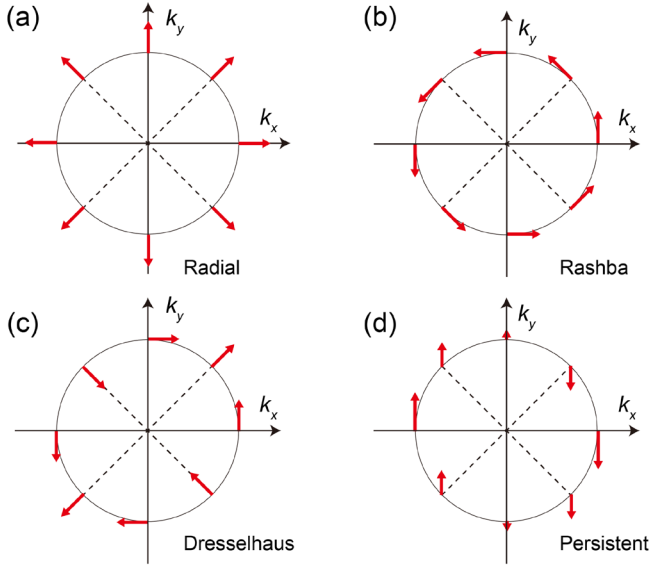


Fig. 1. Spin textures in the momentum space for nonmagnetic materials without inversion symmetry. (a) Radial $\beta_D(\sigma_x k_x + \sigma_y k_y)$, (b) Rashba $\lambda_R(k_x \sigma_y - k_y \sigma_x)$, (c) Dresselhaus $\lambda_D(k_x \sigma_y + k_y \sigma_x)$, (d) persistent $\lambda_R(k_x \sigma_y - k_y \sigma_x) + \lambda_D(k_x \sigma_y + k_y \sigma_x)$ with $\lambda_R = \lambda_D$ here.

Extrinsic parameter method. Since altermagnetic materials are all in symmetry-compensated collinear AFM states with zero net magnetization, it is a natural way to analyze the AHE in terms of the Néel vector \mathbf{n} [8,46,47], where \mathbf{n} is a unit vector ($|\mathbf{n}| = 1$). To determine the profiles of $\sigma_H(\mathbf{n})$, we treat \mathbf{n} as an extrinsic parameter rather than an intrinsic structural parameter in traditional magnetic group method [51,52], and we named it as "extrinsic parameter" method. This approach enables us to analyze the $\sigma_H(\mathbf{n})$ relation in the framework of the nonmagnetic space group. The space group operation $\{R|\mathbf{t}\}$ acting on \mathbf{n} results in the change from $\sigma_H(\mathbf{n})$ to $\sigma_H(\{R|\mathbf{t}\}\mathbf{n})$, and it is equivalent to apply the point symmetry operation R directly on σ_H , i.e.,

$$\sigma_H(\{R|\mathbf{t}\}\mathbf{n}) = R\sigma_H, \quad (1)$$

where the translation operation \mathbf{t} is omitted on the right side, as it does not impact on macroscopic physical properties. Using Eq. (1), we can show that the antiferromagnets, in which two spin sublattices are connected either by inversion P or pure translation $\mathbf{t}_c/2$, do not permit the existence of AHE, because these symmetries only reverse \mathbf{n} not σ_H (Fig. 2(a) and (b)). Coincidentally, the breaking of these two symmetries [13,15,16,19,53] leads to the bands splitting without the spin-orbit coupling (SOC) effect, forming altermagnets. Notably, the spins are fully compensated, meaning the AHE in altermagnets is attributed to intrinsic orbital angular momenta [26].

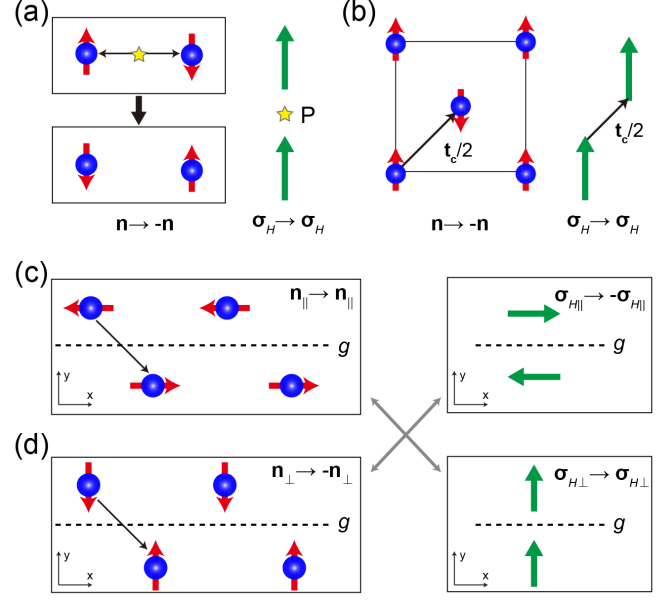


Fig. 2. Transformations of Néel vector \mathbf{n} and anomalous Hall vector σ_H under the (a) inversion symmetry P , (b) $\mathbf{t}_c/2$ translation, and (c, d) glide mirror g operations. The thin arrows between atoms denote the transformations of atom positions under the symmetry operations. The gray cross arrows between (c) and (d) denote the reasonable $\sigma_H - \mathbf{n}$ relationships in altermagnets.

Under mirror or glide mirror symmetry, the relationship between σ_H and \mathbf{n} turns out to be unstraightforward. As shown in Fig. 2(c), when \mathbf{n} is parallel to the glide mirror, the exchange of magnetic atoms with opposite spins preserves the Néel vector \mathbf{n}_{\parallel} (see Sec. I of Supplemental Material [52]). However, the glide mirror reverses the sign of $\sigma_{H\parallel}$. Conversely, when the Néel vector is perpendicular to the glide mirror, the glide mirror operation reverses \mathbf{n}_{\perp} , while leaving the vertical component $\sigma_{H\perp}$ unchanged as it is an axial vector, which is shown in Fig. 2(d). To ensure Eq. (1) holds, σ_H must be perpendicular to \mathbf{n} in the cases of Fig. 2(c, d). Compared to general relationship $\sigma_H \parallel \mathbf{m}$ in ferromagnets, $\sigma_H \perp \mathbf{n}$ relation can emerge in altermagnets [32,37,46,47].

If the directions of the magnetic moments change continuously while remaining strictly anti-parallel between the two spin sublattices, the Néel vector \mathbf{n} traces out a surface resembling a Bloch sphere $|\mathbf{n}| = 1$. We can regard $\sigma_H - \mathbf{n}$ relation as the inner structure of σ_H in the Néel vector space. In Fig. 2 (c, d), we focus on two specific points in the Néel vector space: $\mathbf{n}=(1, 0, 0)$ and $\mathbf{n}=(0, 1, 0)$. Additional symmetries further lead to $\sigma_H(\mathbf{n})$ exhibit unconventional configurations like spin textures in the momentum space. In analogy to the spin texture [48-50], we thus refer to the $\sigma_H - \mathbf{n}$ relationship as the AHNT.

To gain analytical results of $\sigma_H(\mathbf{n})$, we expand σ_H as a Taylor polynomial with respect to \mathbf{n} :

$$\boldsymbol{\sigma}_H(\mathbf{n}) = \mathbf{T}^{(2)} \cdot \mathbf{n} + \mathbf{T}^{(4)} : \mathbf{nnn} + \dots \quad (2)$$

The Taylor expansion is guaranteed because the SOC interaction acts as a perturbation in AHE [8]. The Onsager reciprocal relation allows only the odd terms in Eq. (2), due to its oddness under time-reversal operation. $\mathbf{T}^{(2)}$ and $\mathbf{T}^{(4)}$ are the two-rank and four-rank tensors, respectively. Alternatively, $\boldsymbol{\sigma}_H$ can be expressed in terms of components:

$$\sigma_i = \sum_{j=1}^3 T_{ij}^{(2)} n_j + \sum_{j,k,l=1}^3 T_{ijkl}^{(4)} n_j n_k n_l + \dots \quad (3)$$

The transformation of $\boldsymbol{\sigma}_H$ under the space group operation $\{R|\mathbf{t}\}$ in Eq. (1) becomes:

$$\{R|\mathbf{t}\}: \boldsymbol{\sigma}_H \rightarrow \det |R| D(R) \boldsymbol{\sigma}_H, \quad (4)$$

where $D(R)$ is the matrix of symmetry operation R , and $\det|R|$ is the determinant of $D(R)$. The transformation of the Néel vector \mathbf{n} under $\{R|\mathbf{t}\}$ is given by:

$$\{R|\mathbf{t}\}: \mathbf{n} \rightarrow \pm \det |R| D(R) \mathbf{n}, \quad (5)$$

where the + and - signs indicate whether the two magnetic sublattices with opposite spins are exchanged or not, respectively. Our method properly deals with the transformation of the Néel vector under the symmetry operations (see Eqs. (13, 14) of the Supplemental Material). Although the time-reversal symmetry operation is not explicitly involved in this method, the ± 1 symbol in Eq. (5) essentially reflects the switch of the magnetic moment under time-reversal operation.

With the aid of Eqs. (1)-(5), we can obtain the symmetry-adapted tensors $\mathbf{T}^{(2)}$ and $\mathbf{T}^{(4)}$, and identify the invariant polynomials of \mathbf{n} in Eq. (3). Meanwhile, we have developed an automatically computational code to implement our method (see Sec. II of Supplemental Material [52]).

Classification of AHNTs for altermagnets. With the above extrinsic parameter method, we can conduct a comprehensive study on the $\boldsymbol{\sigma}_H(\mathbf{n})$ relations and corresponding AHNTs in the altermagnets. Since the tensors $\mathbf{T}^{(2)}$ and $\mathbf{T}^{(4)}$ in Eq. (2) resembles the general axial tensors, it suffices to utilize the nonmagnetic group, rather than the magnetic group, to investigate the symmetry constraints imposed on $\mathbf{T}^{(2)}$ and $\mathbf{T}^{(4)}$ in the context of the “extrinsic parameter” method. We found 10 kinds of AHNTs in four categories for altermagnets, based on 10 non-centrosymmetric and non-chiral point groups (see Sec. IV of Supplemental Material [52]).

As summarized in Table I, we find that the altermagnetic materials do not support the radial AHNTs as the ferromagnets. If the symmetry composed on $\boldsymbol{\sigma}_H$ is equivalent to polar group 3m, 6mm, or 4mm, only the Rashba-like AHNT exists. Besides, the pure Dresselhaus AHNTs can only occur if the symmetry composed on $\boldsymbol{\sigma}_H$ identifies with the non-polar tetragonal point group $\bar{4}$, $\bar{4}2m$, or $\bar{4}m2$. Under symmetry constraints equivalent to monoclinic (m) or orthogonal (mm2) group, $\boldsymbol{\sigma}_H(\mathbf{n})$ exhibits a

mixed Rashba and Dresselhaus AHNTs. Interestingly, when the symmetry associated with $\boldsymbol{\sigma}_H$ corresponds to $\bar{6}$, $\bar{6}m2$, or $\bar{4}3m$ point groups, there is no first-order term for $\boldsymbol{\sigma}_H(\mathbf{n})$, resulting in cubic AHNTs as the lowest order in altermagnets. Thus, our classification enables the identification of all AHE behaviors in altermagnets and facilitates the efficient discovery of corresponding materials. Notably, we find a striking similarity between AHNTs and spin textures in momentum space [50,54].

Table I. 10 kinds of AHNTs in four categories for altermagnetic materials. The candidate materials are sourced from the MAGNDATA database [55] and Refs. [15,16,31,56].

AHNT	Expression and equivalent constrained point groups	Candidate materials
Rashba-like	3m, 6mm, 4mm $\boldsymbol{\sigma}_H = A(n_y, -n_x, 0)$	Trigonal: NiCO ₃ , MnCO ₃ , FeCO ₃ , FeF ₃ , CoF ₃ , Fe ₂ O ₃ Tetragonal: Ta ₂ FeB ₂ , KMnF ₃
Dresselhaus-like	$\bar{4}m2$: $\boldsymbol{\sigma}_H = A(n_y, n_x, 0)$ $\bar{4}2m$: $\boldsymbol{\sigma}_H = B(n_x, -n_y, 0)$ $\bar{4}$: $\boldsymbol{\sigma}_H(\bar{4})$ $= \boldsymbol{\sigma}_H(\bar{4}m2) + \boldsymbol{\sigma}_H(\bar{4}2m)$	Tetragonal: RuO ₂ , CoF ₂ , MnF ₂ , NiF ₂ , LiFe ₂ F ₆ , ZrMn ₂ Ge ₄ O ₁₂
Mixed texture	m, mm2 $\boldsymbol{\sigma}_H = (An_y, Bn_x, 0)$ $A \neq \pm B$	Orthogonal: LaMnO ₃ , NdMnO ₃ , ScCrO ₃ , NaOsO ₃ , Cu ₂ V ₂ O ₇ , NiFePO ₅ , Mn ₂ SeO ₃ F ₂
Cubic texture	$\bar{6}$, $\bar{6}m2$ ($\bar{6}2m$), $\bar{4}3m$ $\boldsymbol{\sigma}_H = \mathbf{T}^{(4)} : \mathbf{nnn}$	Hexagonal: MnTe, CrSb, Ba ₃ NiRu ₂ O ₉ , CrNb ₄ S ₈

It should be noted that, similar to the Berry curvature multipoles in reciprocal moment space [57-59] and the multipoles of spin in real space [35,60-62], Eq. (2) can be viewed as the AHE multipoles in the Néel vector space. In Sec. V of Supplemental Material [52], we project $\boldsymbol{\sigma}_H$ to real sphere harmonics and get the corresponding multipoles in the Néel vector space.

Origin of similarity between AHNTs and spin textures. To uncover the symmetry origin of the similarity between AHNTs and spin textures, we consider the general SOC Hamiltonian as: $H_{SOC} = \boldsymbol{\Omega}(\mathbf{k}) \cdot \boldsymbol{\sigma}$, where $\boldsymbol{\sigma} = (\sigma_x, \sigma_y, \sigma_z)$ are the Pauli matrices, and $\boldsymbol{\Omega}(\mathbf{k})$ is a wave-vector dependent spin-orbit field [50], which governs the spin expectation at each \mathbf{k} -point. $\boldsymbol{\Omega}(\mathbf{k})$ behaves as an axial vector, as the AHE conductivity vector $\boldsymbol{\sigma}_H$; whereas, the Néel vector \mathbf{n} is a polar-like vector as the momentum \mathbf{k} , because it switches its sign under the inversion symmetry (see Fig. 2 (a)).

The two similarities result in the fact that point group operations impose equivalent constraints on their forms of corresponding expanded coefficients. For a first-order Taylor expansion, $\boldsymbol{\Omega}(\mathbf{k})$ can be expressed as:

$$\Omega_i(\mathbf{k}) = \sum_{j=1}^3 \mathcal{T}_{ij}^{(2)} k_j, \quad (6)$$

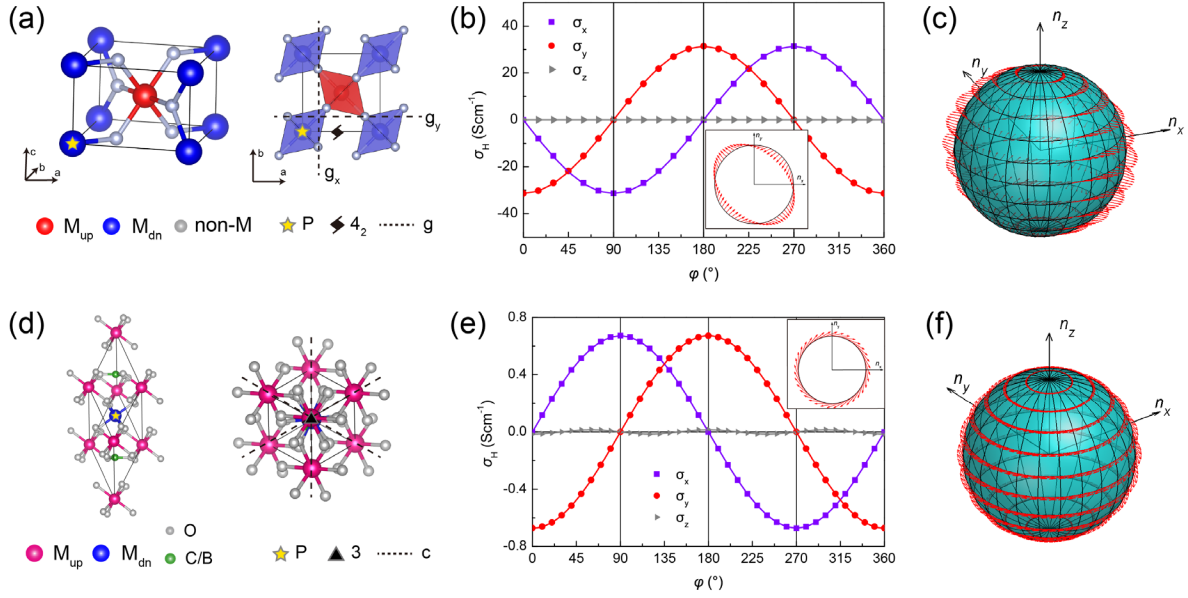


Fig. 3. (a) Crystal structure of rutile-type altermagnetic materials (left: side view, right: top view). (b) Angle dependence of σ_H on \mathbf{n} in the xoy plane. (c) AHNT of rutile-type altermagnet. (d) Crystal structure of calcite-type altermagnets. (e) Corresponding relations of $\sigma_H(\mathbf{n})$ in the xoy plane and (f) AHNT for calcite-type altermagnet.

where the coefficient matrix $\mathcal{T}_{ij}^{(2)}$ is an axial tensor, similar to $\mathbf{T}^{(2)}$ in Eq. (2). For examples, under the polar $3m$, $4mm$ and $6mm$ point groups [54], only two nonzero elements of $\mathcal{T}^{(2)}$ exist: $\mathcal{T}_{xy} = -\mathcal{T}_{yx}$. We can obtain $\mathbf{\Omega}(\mathbf{k}) = \mathcal{T}_{xy}(k_y, -k_x, 0)$ and $H_{SOC} = \mathcal{T}_{xy}(k_y\sigma_x - k_x\sigma_y)$, leading to the Rashba-type spin texture (Fig. 1(b)). It is consistent with AHNTs shown in Table I. The similarity of spin texture and the AHNTs exhibit under all the point groups can be found in Sec. III of the Supplemental Material [52].

Next, we present several typical altermagnets as promising examples to investigate the AHNTs therein. Specifically, we employ an effective tight-binding (TB) model to simulate realistic materials (see Sec. VII of Supplemental Material [52]).

Rutile-type altermagnets with Dresselhaus-like AHNTs. Rutile-type altermagnetic materials, which belong to the space group $P4_2/mnm$ (No. 136), such as RuO_2 [24,26,27,63], NiF_2 , CoF_2 , and MnF_2 [17]. In these AFM materials, the two magnetic atoms occupy the $2a$ sites, specifically at $(0, 0, 0)$ and $(1/2, 1/2, 1/2)$, as illustrated in Fig. 3(a). These two magnetic atoms exhibit a site symmetry of mmm , meaning they are linked by the screw 4_2 , m_z , g_x , and g_y symmetries rather than the inversion symmetry. The symmetry composed on σ_H is equivalent to point group $\bar{4}m2$, and $\sigma_H(\mathbf{n})$ can be written as follows (see Sec. VI of Supplemental Material [52] for detail):

$$\sigma_H(\mathbf{n}) = (An_y, An_x, 0) + O(n^3). \quad (7)$$

The calculated $\sigma_H(\mathbf{n})$ based on the TB model is shown in Fig. 3 (b), where the first-order terms dominate, and σ_x and σ_y oscillate in the sinusoidal and cosine manner with respect to azimuth angle φ in the xoy plane. It is clear that our calculation is consistent with Eq. (7), and also aligns with the previous first-principles calculations of RuO_2 [37], where the specific expression of $\sigma_H(\mathbf{n})$ and AHNT are absent in that work. We can outline the σ_H in the Néel vector space \mathbf{n} , as illustrated in the inset of Fig. 3 (c), which closely resembles the Dresselhaus spin texture in the momentum space.

Except for the rutile-type altermagnets, the Dresselhaus AHNTs can also emerge in the tetragonal $\text{ZrMn}_2\text{Ge}_4\text{O}_{12}$ with the $P4/nbm$ (No. 125) space group and LiFe_2F_6 with $P4_2/mnm$ (No. 136) space group, as listed in Table I.

Calcite-type altermagnets with Rashba-like AHNTs. Altermagnetic materials NiCO_3 , MnCO_3 , FeCO_3 , and FeBO_3 have the calcite structure with $R\bar{3}c$ (No. 167) space group. In this structure, the magnetic atoms occupy the $6b$ positions at $(0, 0, 0)$ and $(1/2, 1/2, 1/2)$, and they are bonded to six equivalent O atoms, forming corner-sharing octahedra, as illustrated in Fig. 3(d). Unlike the 4_2 screw symmetry in the rutile-type altermagnets, the three-fold rotational symmetry present here does not switch the opposite-spin magnetic atoms. Consequently, the symmetry composed on σ_H identify with $3m1$. Using a similar procedure, we derive the corresponding $\sigma_H(\mathbf{n})$ [52]:

$$\sigma_H(\mathbf{n}) = (An_y, -An_x, 0) + O(n^3). \quad (8)$$

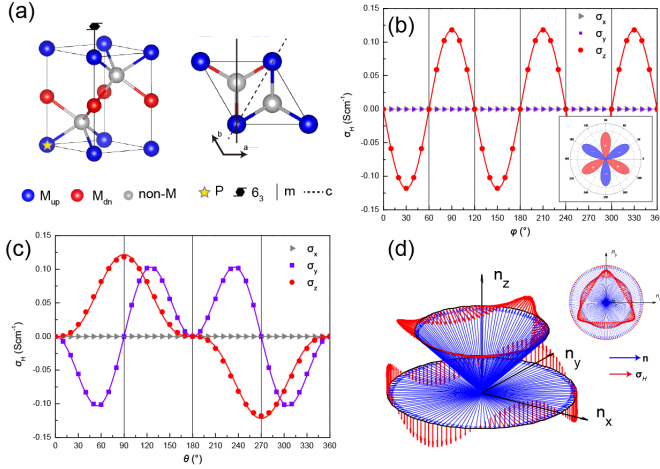


Fig. 4. (a) Crystal structure of NiAs-type altermagnets (left: side view, right: top view). Angle dependence of σ_H in the (b) xoy and (c) yoz plane. Inset in (b) is the magnitude of σ_z with ϕ . The calculated data are fitted by Eq. (9) with lines. (d) AHNT. The insert in (d) shows the top view.

Our numerical results for the effective model are consistent with Eq. (8), as shown in Fig. 3 (e). Due to the m_z mirror symmetry in rutile-type altermagnets which does not switch magnetic atoms, σ_z is vanished when \mathbf{n} is in the xoy plane. It does not exist in calcite altermagnets, which allows σ_z when \mathbf{n} is in the xoy plane and exhibits a small third-order contribution $\sigma_z \sim n_x(n_x^2 - 3n_y^2)$. Although, $\sigma_H(\mathbf{n})$ in xoy plane for the rutile-type (Fig. 3 (b)) and calcite-type (Fig. 3 (e)) altermagnets exhibits similar trigonometric characteristics, essential differences (Eq. (7) and (8)) leading to calcite-type altermagnets hold a Rashba-like AHNT, while the AHNT of rutile-type altermagnets obeys a Dresselhaus-like configuration. This Rashba-like texture ensures that σ_H is always perpendicular to the Néel vector in the (001) plane, a feature of AHNTs that had not been previously recognized. We also outline its AHNT in Fig. 3(f).

In addition to calcite-type altermagnetic materials, altermagnets with trigonal structures such as CaLiOsO_6 , CaLiRuO_6 , $\text{Sr}_3\text{LiRuO}_6$, CoF_3 , and FeF_3 also exhibit $R\bar{3}c$ symmetry, give rise to a similar $\sigma_H(\mathbf{n})$ relation. In fact, the Rashba-type AHNTs are not limited to trigonal altermagnets. For instance, the tetragonal KMnF_3 with the $I4/mcm$ (No. 140) space group and Ta_2FeB_2 [31] with the $P4/mbm$ (No. 127) space group can also display Rashba-like AHNTs, as given in Table I.

If altermagnetic materials lack higher-order rotational n or helical n_q symmetries (where $n \geq 3$), there are no constraints on the coefficients of the first-order Néel vector terms. A mixed AHNTs containing both Rashba and Dresselhaus components hence appears (Table I). For example, perovskite-type altermagnetic materials can exhibit such textures. Additionally, under specific conditions $\lambda_R = \pm\lambda_D$, it is possible to achieve

persistent textures (see Sec. VIII of Supplemental Material [52]). Besides, if the Néel vector is in the xoz (yoz) plane for rutile-type (Eq. (7)) and calcite-type (Eq. (8)) altermagnets, $\sigma_H = (0, An_x, 0)$ [$\sigma_H = (An_y, 0, 0)$], AHNTs of these materials also exhibit persistent characters. It is worth noting that in perovskite-type altermagnetic materials, where each unit cell contains four magnetic atoms, support A-, C-, and G-type AFM configurations. Our extrinsic parameter method effectively characterizes the $\sigma_H(\mathbf{n})$ relations for all three magnetic configurations, validating our approach in complex scenarios.

NiAs-type altermagnets with pure cubic AHNTs. Hexagonal NiAs-type altermagnetic materials include α -MnTe [21,32], CrSb [25,64], etc., which crystallize in the $P6_3/mmc$ (No. 194) space group. In these materials, two opposite-spin magnetic atoms occupy 2a sites at $(0, 0, 0)$ and $(0, 0, 1/2)$. This kind of altermagnetic material exhibits an A-type AFM ground state, where the spins align ferromagnetically within the ab plane and antiferromagnetically between adjacent layers, as shown in Fig. 4(a).

Because the symmetry composed on σ_H is equivalent to $\bar{6}2m$, NiAs-type altermagnets prohibit the first-order Néel vector terms. The σ_H is thus constructed by the third-order term in [52]:

$$\sigma_H(\mathbf{n}) = [2an_xn_yn_z, a(n_x^2 - n_y^2)n_z, c(3n_x^2n_y - n_y^3)], \quad (9)$$

which shows a pure cubic $\sigma_H - \mathbf{n}$ relation, and is associated with the octupole profile in the Néel vector space.

The $\sigma_H(\mathbf{n})$ in the xoy and yoz planes derived from the TB model [52] is presented in Fig. 4 (b) and (c), respectively. The σ_H only has a z -component when \mathbf{n} lies in the xoy plane, and it displays the three-fold rotational symmetry with $\sigma_z = c \sin 3\phi$, as depicted in inset of Fig. 4(b). Our results are in good agreement with both previous theoretical calculations [32,47] and experiments [32,46], where σ_H in the whole Néel vector space is not exposed therein. In the yoz plane (where $n_x=0$), $\sigma_H = [0, -an_y^2n_z, -cn_y^3]$. Therefore, σ_y reaches a minimum at $\theta = \tan^{-1}(\sqrt{2}) \approx 54.7^\circ$, and σ_z is maximized at $\theta = 90^\circ$, as shown in Fig. 4(c). This behavior well aligns with Eq. (9). Finally, we plot its AHNT in Fig. 4(d). Note that our method reveals altermagnets, such as $\text{Ba}_3\text{NiRu}_2\text{O}_9$, and CrNb_4S_8 , with the purely cubic AHNTs, as listed in Table I.

Discussions and conclusion. The above results reveal that the relationships between σ_H and \mathbf{n} are less straightforward and exhibit more intricate behavior compared to those in ferromagnets. Furthermore, by leveraging the property that the σ_H is typically perpendicular to the Néel vector, one can anticipate that in-plane AHE [5-8] is universal in altermagnets. The extrinsic parameter method offers a broader capability to reveal AHE in altermagnets, due to establishing the relationships of $\sigma_H - \mathbf{n}$ in the whole Néel vector space. Additionally, this

method is not only applicable to AHE but can also be extended to other magnetically related physical effects [65], such as the second harmonic generation effect [66], the spin Hall effect [67,68], and nonlinear Hall effect [69-71].

Besides, AHNTs shed light on experimentally detecting the Néel vector in altermagnetic materials via the anomalous Hall transport [52]. Importantly, our results above are also applicable to the magneto-optical effects, because both share similar symmetry requirements. We can utilize the characteristic that the σ_H usually is perpendicular to the Néel vector to design a vertical magneto-optical isolator (see Sec. X of Supplemental Material [52]).

In summary, we develop the “extrinsic parameter” method and algorithm to unveil the relationship between AHE and Néel vector in altermagnets. We present a comprehensive classification of AHNTs for altermagnets, and find a variety of unconventional AHNTs, including Rashba, Dresselhaus, persistent, and pure cubic AHE textures, which are absent in ferromagnetic materials. This complete framework of AHNTs serves as a pictorial category scheme for altermagnets. We found an intriguing similarity between the AHNTs in altermagnets and the spin textures in momentum space, and further elucidated their symmetry origin. Our findings provide a thorough analysis of AHE in altermagnets, and useful guidance for the detection of Néel vectors through AHE, and designing electronic and optoelectronic devices based on altermagnetic materials.

Acknowledgments. We appreciate the helpful discussion with S. M. Zhou, Hua Jiang, Yu Dai, Xiao Li, Ze-Ying Zhang, Zhi-Qiang Zhang, Xiao-Dong Zhou, and Jian-Zhou Zhao. This work was supported by the National Key Research and Development Program of China (Grant No. 2023YFA1406500), the National Natural Science Foundation of China (Grants Nos. 12474100, 12204009, 12204003, and 12174394), and the Natural Science Foundation of Anhui Province (Grant No. 2208085QA08). J. H. was supported by the HFIPS Director’s Fund (Grants No. YZJJQY202304 and No. BJPY2023B05) and Anhui Provincial Major S&T Project (s202305a12020005), the High Magnetic Field Laboratory of Anhui Province under Contract No. AHM-FX-2020-02 and Chinese Academy of Sciences under contract No. JZHKYPT-2021-08. R.-C.X. acknowledges the startup foundation from AHU.

References

- [1] N. Nagaosa, J. Sinova, S. Onoda, A. H. MacDonald, and N. P. Ong, Anomalous Hall effect, *Rev. Mod. Phys.* **82**, 1539 (2010).
- [2] T. Haider, A Review of Magneto-Optic Effects and Its Application, *International Journal of Electromagnetics and Applications* **7**, 17 (2017).
- [3] D. Xiao, M.-C. Chang, and Q. Niu, Berry phase effects on electronic properties, *Rev. Mod. Phys.* **82**, 1959 (2010).
- [4] L. Šmejkal, A. H. MacDonald, J. Sinova, S. Nakatsuji, and T. Jungwirth, Anomalous Hall antiferromagnets, *Nat. Rev. Mat.* **7**, 482 (2022).
- [5] J. Zhou, W. Zhang, Y.-C. Lin, J. Cao, Y. Zhou, W. Jiang, H. Du, B. Tang, J. Shi, B. Jiang *et al.*, Heterodimensional superlattice with in-plane anomalous Hall effect, *Nature* **609**, 46 (2022).
- [6] J. Cao, W. Jiang, X.-P. Li, D. Tu, J. Zhou, J. Zhou, and Y. Yao, In-Plane Anomalous Hall Effect in PT-Symmetric Antiferromagnetic Materials, *Phys. Rev. Lett.* **130**, 166702 (2023).
- [7] W. Peng, Z. Liu, H. Pan, P. Wang, Y. Chen, J. Zhang, X. Yu, J. Shen, M. Yang, Q. Niu *et al.*, Observation of the In-plane Anomalous Hall Effect induced by Octupole in Magnetization Space, arXiv:2402.15741 (2024).
- [8] Z. Liu, M. Wei, D. Hou, Y. Gao, and Q. Niu, Multipolar Anisotropy in Anomalous Hall Effect from Spin-Group Symmetry Breaking, arXiv:2408.08810 (2024).
- [9] J. Železný, Y. Yahagi, C. Gomez-Olivella, Y. Zhang, and Y. Sun, High-throughput study of the anomalous Hall effect, *npj Comput. Mater.* **9**, 151 (2023).
- [10] T. Higo, H. Man, D. B. Gopman, L. Wu, T. Koretsune, O. M. J. van 't Erve, Y. P. Kabanov, D. Rees, Y. Li, M. T. Suzuki *et al.*, Large magneto-optical Kerr effect and imaging of magnetic octupole domains in an antiferromagnetic metal, *Nat. Photonics* **12**, 73 (2018).
- [11] A. L. Balk, N. H. Sung, S. M. Thomas, P. F. S. Rosa, R. D. McDonald, J. D. Thompson, E. D. Bauer, F. Ronning, and S. A. Crooker, Comparing the anomalous Hall effect and the magneto-optical Kerr effect through antiferromagnetic phase transitions in Mn_3Sn , *Appl. Phys. Lett.* **114**, 032401 (2019).
- [12] W. Feng, J. P. Hanke, X. Zhou, G. Y. Guo, S. Blugel, Y. Mokrousov, and Y. Yao, Topological magneto-optical effects and their quantization in noncoplanar antiferromagnets, *Nat. Commun.* **11**, 118 (2020).
- [13] H. Y. Ma, M. Hu, N. Li, J. Liu, W. Yao, J. F. Jia, and J. Liu, Multifunctional antiferromagnetic materials with giant piezomagnetism and noncollinear spin current, *Nat Commun* **12**, 2846 (2021).
- [14] L. Šmejkal, A. B. Hellenes, R. González-Hernández, J. Sinova, and T. Jungwirth, Giant and Tunneling Magnetoresistance in Unconventional Collinear Antiferromagnets with Nonrelativistic Spin-Momentum Coupling, *Phys. Rev. X* **12**, 011028 (2022).
- [15] L. Šmejkal, J. Sinova, and T. Jungwirth, Beyond Conventional Ferromagnetism and Antiferromagnetism: A Phase with Nonrelativistic Spin and Crystal Rotation Symmetry, *Phys. Rev. X* **12**, 031042 (2022).
- [16] L. Šmejkal, J. Sinova, and T. Jungwirth, Emerging Research Landscape of Altermagnetism, *Phys. Rev. X* **12**, 040501 (2022).
- [17] L.-D. Yuan, Z. Wang, J.-W. Luo, E. I. Rashba, and A. Zunger, Giant momentum-dependent spin splitting in

- centrosymmetric low- Z antiferromagnets, *Phys. Rev. B* **102**, 014422 (2020).
- [18] H. Yan, X. Zhou, P. Qin, and Z. Liu, Review on spin-split antiferromagnetic spintronics, *Appl. Phys. Lett.* **124**, 030503 (2024).
- [19] S. Hayami, Y. Yanagi, and H. Kusunose, Bottom-up design of spin-split and reshaped electronic band structures in antiferromagnets without spin-orbit coupling: Procedure on the basis of augmented multipoles, *Phys. Rev. B* **102**, 144441 (2020).
- [20] J. Krempaský, L. Šmejkal, S. W. D'Souza, M. Hajlaoui, G. Springholz, K. Uhlířová, F. Alarab, P. C. Constantinou, V. Strocov, D. Usanov *et al.*, Altermagnetic lifting of Kramers spin degeneracy, *Nature* **626**, 517 (2024).
- [21] S. Lee, S. Lee, S. Jung, J. Jung, D. Kim, Y. Lee, B. Seok, J. Kim, B. G. Park, L. Šmejkal *et al.*, Broken Kramers Degeneracy in Altermagnetic MnTe, *Phys. Rev. Lett.* **132**, 036702 (2024).
- [22] T. Osumi, S. Souma, T. Aoyama, K. Yamauchi, A. Honma, K. Nakayama, T. Takahashi, K. Ohgushi, and T. Sato, Observation of a giant band splitting in altermagnetic MnTe, *Phys. Rev. B* **109**, 115102 (2024).
- [23] Y.-P. Zhu, X. Chen, X.-R. Liu, Y. Liu, P. Liu, H. Zha, G. Qu, C. Hong, J. Li, Z. Jiang *et al.*, Observation of plaid-like spin splitting in a noncoplanar antiferromagnet, *Nature* **626**, 523 (2024).
- [24] O. Fedchenko, J. Minár, A. Akashdeep, S. W. D'Souza, D. Vasilyev, O. Tkach, L. Odenbreit, Q. Nguyen, D. Kutnyakhov, N. Wind *et al.*, Observation of time-reversal symmetry breaking in the band structure of altermagnetic RuO₂, *Sci. Adv.* **10**, ead4883 (2024).
- [25] S. Reimers, L. Odenbreit, L. Šmejkal, V. N. Strocov, P. Constantinou, A. B. Hellenes, R. Jaeschke Ubierno, W. H. Campos, V. K. Bharadwaj, A. Chakraborty *et al.*, Direct observation of altermagnetic band splitting in CrSb thin films, *Nat. Commun.* **15**, 2116 (2024).
- [26] L. Šmejkal, R. González-Hernández, T. Jungwirth, and J. Sinova, Crystal time-reversal symmetry breaking and spontaneous Hall effect in collinear antiferromagnets, *Sci. Adv.* **6**, eaaz8809 (2020).
- [27] Z. Feng, X. Zhou, L. Šmejkal, L. Wu, Z. Zhu, H. Guo, R. González-Hernández, X. Wang, H. Yan, P. Qin *et al.*, An anomalous Hall effect in altermagnetic ruthenium dioxide, *Nat. Electron.* **5**, 735 (2022).
- [28] I. I. Mazin, K. Koepf, M. D. Johannes, R. González-Hernández, and L. Šmejkal, Prediction of unconventional magnetism in doped FeSb₂, *Prog. Nat. Sci.* **118**, e2108924118 (2021).
- [29] M. Naka, Y. Motome, and H. Seo, Anomalous Hall effect in antiferromagnetic perovskites, *Phys. Rev. B* **106**, 195149 (2022).
- [30] T. P. T. Nguyen and K. Yamauchi, Ab initio prediction of anomalous Hall effect in antiferromagnetic CaCrO₃, *Phys. Rev. B* **107**, 155126 (2023).
- [31] X.-Y. Hou, H.-C. Yang, Z.-X. Liu, P.-J. Guo, and Z.-Y. Lu, Large intrinsic anomalous Hall effect in both Nb₂FeB₂ and Ta₂FeB₂ with collinear antiferromagnetism, *Phys. Rev. B* **107**, L161109 (2023).
- [32] R. D. Gonzalez Betancourt, J. Zubáč, R. Gonzalez-Hernandez, K. Geishendorf, Z. Šobáň, G. Springholz, K. Olejník, L. Šmejkal, J. Sinova, T. Jungwirth *et al.*, Spontaneous Anomalous Hall Effect Arising from an Unconventional Compensated Magnetic Phase in a Semiconductor, *Phys. Rev. Lett.* **130**, 036702 (2023).
- [33] L. Han, X. Fu, R. Peng, X. Cheng, J. Dai, L. Liu, Y. Li, Y. Zhang, W. Zhu, H. Bai *et al.*, Electrical 180° switching of Néel vector in spin-splitting antiferromagnet, *Sci. Adv.* **10**, eadn0479 (2024).
- [34] X. Zhou, W. Feng, R.-W. Zhang, L. Šmejkal, J. Sinova, Y. Mokrousov, and Y. Yao, Crystal Thermal Transport in Altermagnetic RuO₂, *Phys. Rev. Lett.* **132**, 056701 (2024).
- [35] S. Hayami and H. Kusunose, Essential role of the anisotropic magnetic dipole in the anomalous Hall effect, *Phys. Rev. B* **103**, L180407 (2021).
- [36] T. Sato, S. Haddad, I. C. Fulga, F. F. Assaad, and J. van den Brink, Altermagnetic Anomalous Hall Effect Emerging from Electronic Correlations, *Phys. Rev. Lett.* **133**, 086503 (2024).
- [37] X. Zhou, W. Feng, X. Yang, G.-Y. Guo, and Y. Yao, Crystal chirality magneto-optical effects in collinear antiferromagnets, *Phys. Rev. B* **104**, 024401 (2021).
- [38] I. V. Solovyev, Magneto-optical effect in the weak ferromagnets LaMO₃ (M= Cr, Mn, and Fe), *Phys. Rev. B* **55**, 8060 (1997).
- [39] B. Pan, P. Zhou, P. Lyu, H. Xiao, X. Yang, and L. Sun, General Stacking Theory for Altermagnetism in Bilayer Systems, *Phys. Rev. Lett.* **133**, 166701 (2024).
- [40] Y. Fang, J. Cano, and S. A. A. Ghorashi, Quantum Geometry Induced Nonlinear Transport in Altermagnets, *Phys. Rev. Lett.* **133**, 106701 (2024).
- [41] L. Šmejkal, A. Marmodoro, K.-H. Ahn, R. González-Hernández, I. Turek, S. Mankovsky, H. Ebert, S. W. D'Souza, O. Šipr, J. Sinova *et al.*, Chiral Magnons in Altermagnetic RuO₂, *Phys. Rev. Lett.* **131**, 256703 (2023).
- [42] J. A. Ouassou, A. Brataas, and J. Linder, dc Josephson Effect in Altermagnets, *Phys. Rev. Lett.* **131**, 076003 (2023).
- [43] Z. Jin, Z. Zeng, Y. Cao, and P. Yan, Skyrmion Hall Effect in Altermagnets, *Phys. Rev. Lett.* **133**, 196701 (2024).
- [44] S.-B. Zhang, L.-H. Hu, and T. Neupert, Finite-momentum Cooper pairing in proximitized altermagnets, *Nat. Commun.* **15**, 1801 (2024).
- [45] O. Gomonay, V. P. Kravchuk, R. Jaeschke-Ubierno, K. V. Yershov, T. Jungwirth, L. Šmejkal, J. v. d. Brink, and J. Sinova, Structure, control, and dynamics of altermagnetic textures, *npj Spintronics* **2**, 35 (2024).
- [46] R. D. Gonzalez Betancourt, J. Zubáč, K. Geishendorf, P. Ritzinger, B. Růžicková, T. Kotte, J. Železný, K. Olejník, G. Springholz, B. Büchner *et al.*, Anisotropic magnetoresistance in altermagnetic MnTe, *npj Spintronics* **2**, 45 (2024).

- [47] P. A. McClarty and J. G. Rau, Landau Theory of Altermagnetism, *Phys. Rev. Lett.* **132**, 176702 (2024).
- [48] A. Manchon, H. C. Koo, J. Nitta, S. M. Frolov, and R. A. Duine, New perspectives for Rashba spin-orbit coupling, *Nat. Mater.* **14**, 871 (2015).
- [49] J. Schliemann, Colloquium: Persistent spin textures in semiconductor nanostructures, *Rev. Mod. Phys.* **89**, 011001 (2017).
- [50] L. L. Tao and E. Y. Tsymbal, Perspectives of spin-textured ferroelectrics, *J. Phys. D: Appl. Phys.* **54**, 113001 (2021).
- [51] S. V. Gallego, J. Etxebarria, L. Elcoro, E. S. Tasci, and J. M. Perez-Mato, Automatic calculation of symmetry-adapted tensors in magnetic and non-magnetic materials: a new tool of the Bilbao Crystallographic Server, *Acta Crystallogr. A Found Adv.* **75**, 438 (2019).
- [52] See Supplemental Material at <http://xxx> for detailed information on the extrinsic parameter method, the comparison of spin texture and anomalous Hall texture, effective TB models, and calculation method, AHNTs of perovskite-type altermagnetic materials, which includes Refs. [72-80].
- [53] L.-D. Yuan, A. B. Georgescu, and J. M. Rondinelli, Nonrelativistic Spin Splitting at the Brillouin Zone Center in Compensated Magnets, *Phys. Rev. Lett.* **133**, 216701 (2024).
- [54] C. Mera Acosta, L. Yuan, G. M. Dalpian, and A. Zunger, Different shapes of spin textures as a journey through the Brillouin zone, *Phys. Rev. B* **104**, 104408 (2021).
- [55] S. V. Gallego, J. M. Perez-Mato, L. Elcoro, E. S. Tasci, R. M. Hanson, K. Momma, M. I. Aroyo, and G. Madariaga, MAGNDATA: towards a database of magnetic structures. I. The commensurate case, *J. Appl. Crystallogr.* **49**, 1750 (2016).
- [56] Y. Guo, H. Liu, O. Janson, I. C. Fulga, J. van den Brink, and J. I. Facio, Spin-split collinear antiferromagnets: A large-scale ab-initio study, *Matter. Today Phys.* **32**, 100991 (2023).
- [57] I. Sodemann and L. Fu, Quantum Nonlinear Hall Effect Induced by Berry Curvature Dipole in Time-Reversal Invariant Materials, *Phys. Rev. Lett.* **115**, 216806 (2015).
- [58] R.-C. Xiao, D.-F. Shao, W. Huang, and H. Jiang, Electrical detection of ferroelectriclike metals through the nonlinear Hall effect, *Phys. Rev. B* **102**, 024109 (2020).
- [59] Z. Z. Du, H.-Z. Lu, and X. C. Xie, Nonlinear Hall effects, *Nat. Rev. Phys.* **3**, 744 (2021).
- [60] M. T. Suzuki, T. Koretsune, M. Ochi, and R. Arita, Cluster multipole theory for anomalous Hall effect in antiferromagnets, *Phys. Rev. B* **95**, 094406 (2017).
- [61] M. Yatsushiro, H. Kusunose, and S. Hayami, Multipole classification in 122 magnetic point groups for unified understanding of multiferroic responses and transport phenomena, *Phys. Rev. B* **104**, 054412 (2021).
- [62] S. Bhowal and N. A. Spaldin, Ferroically Ordered Magnetic Octupoles in d-Wave Altermagnets, *Phys. Rev. X* **14**, 011019 (2024).
- [63] D. F. Shao, S. H. Zhang, M. Li, C. B. Eom, and E. Y. Tsymbal, Spin-neutral currents for spintronics, *Nat. Commun.* **12**, 7061 (2021).
- [64] J. Ding, Z. Jiang, X. Chen, Z. Tao, Z. Liu, T. Li, J. Liu, J. Sun, J. Cheng, J. Liu *et al.*, Large Band Splitting in g-Wave Altermagnet CrSb, *Phys. Rev. Lett.* **133**, 206401 (2024).
- [65] R.-C. Xiao, TensorSymmetry: a package to get the symmetry-adapted tensors in magnetic and non-magnetic materials (to be published).
- [66] R.-C. Xiao, D.-F. Shao, W. Gan, H.-W. Wang, H. Han, Z. G. Sheng, C. Zhang, H. Jiang, and H. Li, Classification of second harmonic generation effect in magnetically ordered materials, *npj Quantum Mater.* **8**, 62 (2023).
- [67] R. Gonzalez-Hernandez, L. Smejkal, K. Vyborny, Y. Yahagi, J. Sinova, T. Jungwirth, and J. Zelezny, Efficient Electrical Spin Splitter Based on Nonrelativistic Collinear Antiferromagnetism, *Phys. Rev. Lett.* **126**, 127701 (2021).
- [68] H. Bai, Y. C. Zhang, Y. J. Zhou, P. Chen, C. H. Wan, L. Han, W. X. Zhu, S. X. Liang, Y. C. Su, X. F. Han *et al.*, Efficient Spin-to-Charge Conversion via Altermagnetic Spin Splitting Effect in Antiferromagnet RuO₂, *Phys. Rev. Lett.* **130**, 216701 (2023).
- [69] D.-F. Shao, S.-H. Zhang, G. Gurung, W. Yang, and E. Y. Tsymbal, Nonlinear Anomalous Hall Effect for Neel Vector Detection, *Phys. Rev. Lett.* **124**, 067203 (2020).
- [70] H. Liu, J. Zhao, Y.-X. Huang, W. Wu, X.-L. Sheng, C. Xiao, and S. A. Yang, Intrinsic Second-Order Anomalous Hall Effect and Its Application in Compensated Antiferromagnets, *Phys. Rev. Lett.* **127**, 277202 (2021).
- [71] C. Wang, Y. Gao, and D. Xiao, Intrinsic Nonlinear Hall Effect in Antiferromagnetic Tetragonal CuMnAs, *Phys. Rev. Lett.* **127**, 277201 (2021).
- [72] H. Pan, H. Li, J. Huang, Z. Liu, M. Fang, Y. Yuan, D. Liu, X. Hu, W. Peng, Z. Liang *et al.*, Orthogonal Geometry of Magneto-Optical Kerr Effect Enabled by Magnetization Multipole of Berry Curvature, *arXiv:2412.09857* (2024).
- [73] J. Železný, H. Gao, A. Manchon, F. Freimuth, Y. Mokrousov, J. Zemen, J. Mašek, J. Sinova, and T. Jungwirth, Spin-orbit torques in locally and globally noncentrosymmetric crystals: Antiferromagnets and ferromagnets, *Phys. Rev. B* **95**, 014403 (2017).
- [74] Xiaobing Chen, Yuntian Liu, Pengfei Liu, Yutong Yu, J. L. Jun Ren, Ao Zhang, and Q. Liu, Catalog of Unconventional Magnons in Collinear Magnets, *arXiv:2307.12366* (2023).
- [75] Z. Zhang, Z.-M. Yu, G.-B. Liu, and Y. Yao, MagneticTB: A package for tight-binding model of magnetic and non-magnetic materials, *Comput. Phys. Commun.* **270**, 108153 (2022).
- [76] M. e. Roig, A. Kreisel, Y. Yu, B. M. Andersen, and D. F. Agterberg, Minimal Models for Altermagnetism, *arXiv:2402.15616* (2024).
- [77] D. J. Wang, J. R. Sun, S. Y. Zhang, G. J. Liu, B. G. Shen, H. F. Tian, and J. Q. Li, Hall effect in La_{0.7}Ce_{0.3}MnO_{3+δ} films with variable oxygen content, *Phys. Rev. B* **73**, 144403 (2006).

- [78] K. Li, R. Cheng, Z. Chen, J. Fang, X. Cao, and Y. Zhang, Anomalous Hall conductivity and magnetoresistance in epitaxial $\text{La}_{0.67}\text{Ca}_{0.33}\text{MnO}_{3-\delta}$ thin films, *J. Appl. Phys.* **84**, 1467 (1998).
- [79] T. Asaba, Z. Xiang, T. H. Kim, M. S. Rzechowski, C. B. Eom, and L. Li, Unconventional ferromagnetism in epitaxial (111) LaNiO_3 , *Phys. Rev. B* **98**, 121105 (2018).
- [80] M.-W. Yoo, J. Tornos, A. Sander, L.-F. Lin, N. Mohanta, A. Peralta, D. Sanchez-Manzano, F. Gallego, D. Haskel, J. W. Freeland *et al.*, Large intrinsic anomalous Hall effect in SrIrO_3 induced by magnetic proximity effect, *Nat. Commun.* **12**, 3283 (2021).

SUPPLEMENTAL MATERIAL

Anomalous-Hall Néel textures in altermagnetic materials

Rui-Chun Xiao,^{1,2,*} Hui Li,^{1,2} Hui Han,^{1,2} Wei Gan,¹ Mengmeng Yang,^{1,2} Ding-Fu Shao,³ Shu-Hui Zhang,⁴
Yang Gao,⁵ Mingliang Tian,^{6,7,†} Jianhui Zhou^{6,‡}

¹*Institute of Physical Science and Information Technology, Anhui University, Hefei 230601, China*

²*Anhui Provincial Key Laboratory of Magnetic Functional Materials and Devices, School of Materials Science and Engineering, Anhui University, Hefei 230601, China*

³*Key Laboratory of Materials Physics, Institute of Solid State Physics, Chinese Academy of Sciences, 230031 Hefei, China*

⁴*College of Mathematics and Physics, Beijing University of Chemical Technology, Beijing 100029, China*

⁵*Department of Physics, University of Science and Technology of China, Hefei 230026, China.*

⁶*Anhui Key Laboratory of Low-Energy Quantum Materials and Devices, High Magnetic Field Laboratory, HFIPS, Anhui, Chinese Academy of Sciences, Hefei, Anhui 230031, China.*

⁷*School of Physics and Optoelectronics Engineering, Anhui University, Hefei 230601, China*

^{*}xiaoruichun@ahu.edu.cn; [†]mltian@ahu.edu.cn; [‡]jhzhou@hmfl.ac.cn

Section I. Transformations of Néel vector under the space group operations

The transformations of the Néel vector under the space group operation are illustrated in Fig. S1. The spin remains invariant under the translation operation, therefore $\mathbf{t}_c/2$ (\mathbf{t}_c equals the integral lattice vectors) operation, which connects magnetic atoms with opposite spins, reverses the Néel vectors, as shown in Fig. S1(a). As an axial vector, the spin reverses when parallel to the glide mirror (Fig. S1(b)), and remains invariant when perpendicular to the glide mirror (Fig. S1(c)), resulting in the invariant and reverse of Néel vectors, respectively.

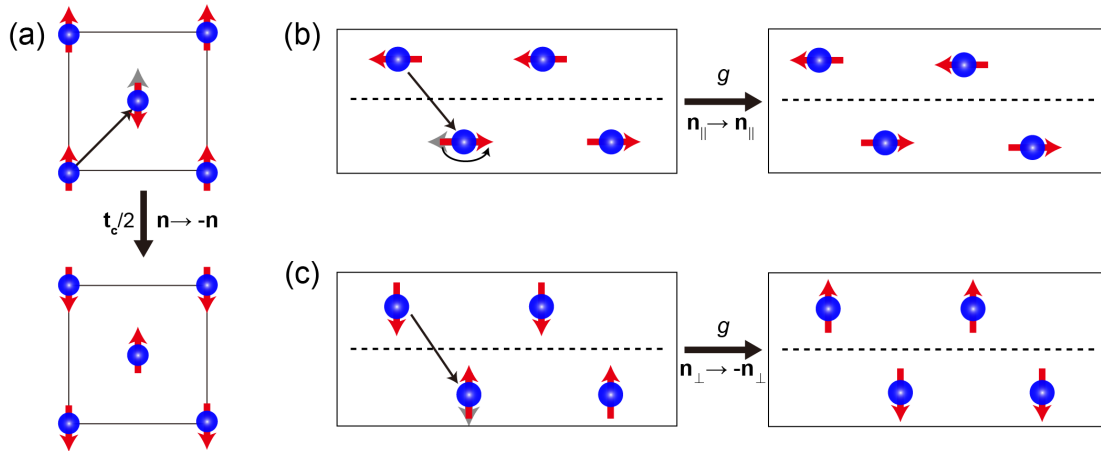


Fig. S1. (a) Transformation of Néel vector under the $\mathbf{t}_c/2$ translation operation. (b) Transformations of the (b) horizontal and (c) vertical components of Néel vectors under the glide mirror operation.

Section II. Extrinsic parameter method and algorithm

First, we investigate the relationship between the anomalous Hall conductivity vector $\boldsymbol{\sigma}_H$ and the Néel vector \mathbf{n} at first-order Taylor approximation. Under this situation, $\boldsymbol{\sigma}_H$ can be expanded in the following form:

$$\begin{cases} \sigma_x = T_{xx}n_x + T_{xy}n_y + T_{xz}n_z, \\ \sigma_y = T_{yx}n_x + T_{yy}n_y + T_{yz}n_z, \\ \sigma_z = T_{zx}n_x + T_{zy}n_y + T_{zz}n_z. \end{cases} \quad (10)$$

This indicates that the anomalous Hall vector $\boldsymbol{\sigma}_H$ and the Néel vector \mathbf{n} are connected by a 3×3 tensor, expressed as:

$$\sigma_i = (\mathbf{T}^{(2)} \cdot \mathbf{n})_i = \sum_j T_{ij}^{(2)} n_j. \quad (11)$$

Here, $\mathbf{T}^{(2)}$ is a two-dimensional tensor whose elements are in Eq. (10), *i.e.*,

$$\mathbf{T}^{(2)} = \begin{bmatrix} T_{xx} & T_{xy} & T_{xz} \\ T_{yx} & T_{yy} & T_{yz} \\ T_{zx} & T_{zy} & T_{zz} \end{bmatrix}. \quad (12)$$

Under the space group operation $\{R | \mathbf{t}\}$, $\boldsymbol{\sigma}_H$ and \mathbf{n} are transformed into $\boldsymbol{\sigma}'_H$ and \mathbf{n}' , which obey the following relationship:

$$\boldsymbol{\sigma}'_H = \det(R)D(R)\boldsymbol{\sigma}_H, \quad (13)$$

$$\mathbf{n}' = \pm \det(R)D(R)\mathbf{n}, \quad (14)$$

where $D(R)$ is the matrix form of point symmetry operation R . If $\{R | \mathbf{t}\}$ does not exchange magnetic atoms with opposite spins, we take the positive sign in Eq. (14); if $\{R | \mathbf{t}\}$ switches magnetic atoms with opposite spins, we take the negative sign. This can be expressed as:

$$\{R | \mathbf{t}\} \mathbf{r}_{i,\uparrow} = R\mathbf{r}_{i,\uparrow} + \mathbf{t} \begin{cases} = \mathbf{r}_{j,\uparrow} + (n_1\mathbf{a} + n_2\mathbf{b} + n_3\mathbf{c}), & +1 \\ = \mathbf{r}_{j,\downarrow} + (n_1\mathbf{a} + n_2\mathbf{b} + n_3\mathbf{c}), & -1 \end{cases} \quad (15)$$

where \mathbf{a} , \mathbf{b} , and \mathbf{c} are the lattice vectors in three directions, n_1 , n_2 , and n_3 are integers.

Similar to Eq. (11), the transformed vectors $\boldsymbol{\sigma}'_H$ and \mathbf{n}' satisfy the relationship: $\boldsymbol{\sigma}'_H = \mathbf{T}'^{(2)} \cdot \mathbf{n}'$. Thus, $\mathbf{T}'^{(2)}$ and $\mathbf{T}^{(2)}$ must satisfy the following transformation relationship:

$$\mathbf{T}'^{(2)} = \pm D(R)\mathbf{T}^{(2)}D(R^{-1}). \quad (16)$$

In Eq. (16), $\det(R)$ is eliminated because both sides of the equation all have axial vectors. Furthermore, Eq. (16) can also be expressed in summation form

$$T'_{ij}{}^{(2)} = \pm \sum_{mn} R_{im} R_{jn} T_{mn}{}^{(2)}, \quad (17)$$

where R_{ij} is an element of the matrix $D(R)$.

If the anomalous Hall vector $\boldsymbol{\sigma}_H$ is further expanded to the third-order terms of the Néel vector \mathbf{n} , similar to Eq. (11), it can be expressed with a fourth-order tensor:

$$\boldsymbol{\sigma}_H = \mathbf{T}^{(4)} : \mathbf{nnn}. \quad (18)$$

Analogous to Eq. (17), the transformation of the fourth-dimensional tensor $\mathbf{T}^{(4)}$ under symmetry operations is given by:

$$T_{ijkl}^{(4)} = \pm R_{im} R_{jn} R_{kp} R_{lq} T_{mnpq}^{(4)}. \quad (19)$$

Additionally, since the expression in Eq. (18) involves the multiplication of three Néel vectors, $\mathbf{T}^{(4)}$ exhibits commutative symmetry for the last three indices:

$$T_{ijkl}^{(4)} = T_{ijlk}^{(4)} = T_{ikjl}^{(4)} = T_{iklj}^{(4)} = T_{ilkj}^{(4)} = T_{iljk}^{(4)}. \quad (20)$$

As a result, the number of independent tensor elements of $\mathbf{T}^{(4)}$ decreases from $3^4=81$ to 30.

Considering both the first-order and third-order Taylor expansions of \mathbf{n} , the $\boldsymbol{\sigma}_H$ can ultimately be expressed as:

$$\sigma_i(\mathbf{n}) = \sum_{j=1}^3 T_{ij}^{(2)} n_j + \sum_{j,k,l=1}^3 T_{ijkl}^{(4)} n_j n_k n_l. \quad (21)$$

```

Clear["Global`*"]
Get[NotebookDirectory[] <> "\\Script\\" <> "SGData.wl"]
Get[NotebookDirectory[] <> "\\Script\\" <> "AHENeel.wl"]

{SGop, Basis} = SpaceGroupData[194]; (*NiAs type*)
Magup = {{0, 0, 0}}; (*Magnetic atom position with spin up state,in crystal coordinate*)
Magdn = {{0, 0, 1/2}}; (*Magnetic atom position with spin down state,in crystal coordinate*)
sigma = AHENeel[SGop, Basis, Magup];

Space group name: P6_3/mmc
Bravais lattice type: HexagonalP

Conventional Lattice Vectors: {{a, 0, 0}, {-a/2, sqrt(3)a/2, 0}, {0, 0, c}}

Primitive Lattice Vectors: {{a, 0, 0}, {-a/2, sqrt(3)a/2, 0}, {0, 0, c}}

sigma_H = (0, 0, 0) + ( (6 n_x n_y n_z T_xxyz,
                      3 n_x^2 n_z T_xxyz - 3 n_y^2 n_z T_xxyz,
                      3 n_x^2 n_y T_zxxy - n_y^3 T_zxxy) )

Independent 1st order terms: {}, Number:0
Independent 3rd order terms: {T_xxyz, T_zxxy}, Number:2

```

Fig. S2. Usage of Mathematica code “AHE-texture” to determine the $\boldsymbol{\sigma}_H(\mathbf{n})$ relation.

Based on Eq. (17) and Eq. (19), we have developed the corresponding computational code “AHE-texture” based on Wolfram Mathematica, which was shared on GitHub (<https://github.com/Ruichun/AHE-texture>). The usage of code is shown in Fig. S2. Firstly, we load the code, then input the space group number and the positions of the magnetic atoms with spin-up and spin-down states. After running the codes, the Taylor expansion

polynomials of anomalous Hall vector $\boldsymbol{\sigma}_H$ with \mathbf{n} , as well as the independent tensor elements, will be outputted automatically.

Although our research focuses on altermagnets, the proposed method is also suitable for ferromagnets. To illustrate this point, we have successfully derived the anomalous Hall conductivity for Fe (space group $Im\bar{3}m$) as a function of its magnetic moment:

$$\boldsymbol{\sigma}_H = \begin{pmatrix} T_{Xx} m_x \\ T_{Xx} m_y \\ T_{Xx} m_z \end{pmatrix} + \begin{pmatrix} T_{Xxxx} m_x^3 + 3T_{Xxyy} m_x m_y^2 + 3T_{Xxyy} m_x m_z^2 \\ T_{Xxxx} m_y^3 + 3T_{Xxyy} m_x^2 m_y + 3T_{Xxyy} m_z^2 m_y \\ T_{Xxxx} m_z^3 + 3T_{Xxyy} m_x^2 m_z + 3T_{Xxyy} m_y^2 m_z \end{pmatrix} = A \begin{pmatrix} m_x \\ m_y \\ m_z \end{pmatrix} + B \begin{pmatrix} m_x^3 \\ m_y^3 \\ m_z^3 \end{pmatrix}, \quad (22)$$

where $A = T_{Xx} + 3T_{Xxyy}$, $B = T_{Xxxx} - 3T_{Xxyy}$, $\mathbf{m} = (m_x, m_y, m_z)$ is the magnetic moment vector with $m_x^2 + m_y^2 + m_z^2 = 1$. The above result is well consistent with previously reported outcomes in Refs. [1-3].

Unlike the traditional magnetic group method that treats both the magnetic moment and crystal structure as intrinsic parameters, we instead analyze the Néel vector as an extrinsic parameter. It should be noted that the traditional magnetic group methods are limited to determine the direction of $\boldsymbol{\sigma}_H$ for specific crystalline orientations (see Sec. IX). Readers can refer to the MTENSOR module in Bilbao Crystallographic Server (<https://www.cryst.ehu.es/cgi-bin/cryst/programs/mtensor.pl>, and corresponding theory presented Ref. [4]) for more information. In contrast, the extrinsic parameter method offers a broader capability, enabling the establishment of relationships among different magnetic orientations. Besides, the ‘‘extrinsic parameter’’ method only considers the symmetry operations of space groups. Although this method does not directly involve time-reversal symmetry operation like the magnetic groups, it is noteworthy that the ± 1 symbol in Eq. (14) essentially reflects the sign change of the magnetic moment under time-reversal operation.

Besides, the linear-response-symmetry code (<https://bitbucket.org/zeleznyj/linear-response-symmetry/src/master/>, and corresponding theory presented in Ref. [5]) is the pioneering work on determining various symmetry properties of magnetic and nonmagnetic crystals. With the aid of the site point group symmetry, this approach enables us to derive the response tensors through a Taylor expansion of the magnetic moment. This method demonstrates remarkable efficiency in determining the response tensors for ferromagnetic systems. On the other hand, ‘‘in a two-sublattice collinear antiferromagnet, if a projection on one of the magnetic atoms is specified, then this expansion also applies. In general, however, for a collinear antiferromagnet the expansion is different from a ferromagnet and this is not implemented!’’, as stated on its official website. This unimplemented functionality for antiferromagnetic materials in linear-response-symmetry

code calls for effective and convenient methods to handle the transformation of the magnetic order parameters under symmetry operations.

The comparison of linear-response-symmetry, extrinsic parameter method, and magnetic group method are summarized in Table SI.

Table SI The comparison of linear-response-symmetry, extrinsic parameter method, and Bilbao Crystallographic Server.

	Linear-response-symmetry code	Extrinsic parameter method	Magnetic group method
Group	Site point group	Space group	Magnetic group
Suitable materials	Ferromagnets or one sublattice in antiferromagnets	Ferromagnets and (collinear) antiferromagnets	All the magnets
Order parameter	Magnetic moment	Magnetic moment or Néel vector	× Not available

Section III. The comparison of spin texture and anomalous Hall texture

In nonmagnetic materials, the combination of the SOC effect and the breaking of inversion symmetry induces spin splitting of electronic bands, leading to the spin texture in reciprocal momentum space. Similarly, AHE arises from SOC effect [3] and time-reversal symmetry breaking.

The SOC Hamiltonian is given by $H_{SOC} = \Omega(\mathbf{k}) \cdot \boldsymbol{\sigma}$, where $\boldsymbol{\sigma} = (\sigma_x, \sigma_y, \sigma_z)$ are the Pauli matrices, and $\Omega(\mathbf{k})$ is a wave-vector dependent spin-orbit field [6]. $\Omega(\mathbf{k})$ governs the spin at each \mathbf{k} -point. $\Omega(\mathbf{k})$ behaves as a pseudovector, as the AHE conductivity vector $\boldsymbol{\sigma}_H$. For a first-order Taylor expansion of wave vector \mathbf{k} , $\Omega(\mathbf{k})$ can be expressed as:

$$\Omega_i(\mathbf{k}) = \sum_{j=1}^3 \mathcal{T}_{ij}^{(2)} k_j. \quad (23)$$

where the 1st Taylor expansion coefficient matrix $[\mathcal{T}_{ij}^{(2)}]$ forms an axial tensor. The symmetry constraining on any axial tensor is the same:

$$\mathcal{T}^{(2)} = \det(R)D(R)\mathcal{T}^{(2)}D(R^{-1}). \quad (24)$$

For example, under the polar $3m$, $4mm$, and $6mm$ point groups, we can obtain the symmetry-constrained $\mathcal{T}^{(2)}$ based on Eq. (24) as follows

$$\left. \begin{array}{l} 3m \\ 4mm \\ 6mm \end{array} \right\} : \mathcal{T}^{(2)} = \begin{pmatrix} 0 & \mathcal{T}_{xy} & 0 \\ -\mathcal{T}_{xy} & 0 & 0 \\ 0 & 0 & 0 \end{pmatrix}. \quad (25)$$

Putting Eq. (25) to (23), we can obtain the SOC vector field $\Omega(\mathbf{k}) = \lambda_R(-k_y, k_x, 0)$ ($\lambda_R = -\mathcal{T}_{xy}$), consequently $H_{SOC} = \lambda_R(k_x\sigma_y - k_y\sigma_x)$, leading to the Rashba-type spin texture. Similarly, under the chiral point group $\bar{4}m2$, the expression of $\mathcal{T}^{(2)}$ is

$$\bar{4}m2: \mathcal{T}^{(2)} = \begin{pmatrix} 0 & \mathcal{T}_{xy} & 0 \\ \mathcal{T}_{xy} & 0 & 0 \\ 0 & 0 & 0 \end{pmatrix}. \quad (26)$$

Putting Eq. (26) to (23), we can obtain $\Omega(\mathbf{k}) = \beta_D(k_y, k_x, 0)$ ($\beta_D = \mathcal{T}_{xy}$), consequently $H_{SOC} = \beta_D(k_x\sigma_y + k_y\sigma_x)$, leading to the Dresshaus-type spin texture. Under the $\bar{6}$, $\bar{6}m2$ ($\bar{6}2m$), and $\bar{4}3m$ point groups, the existence of $\mathcal{T}^{(2)}$ is not allowed. Therefore, there is no first-order term of $\Omega(\mathbf{k})$, resulting in pure cubic spin texture. The above results are consistent with Ref. [7]. The results presented above resemble the outcomes depicted in the AHE texture in Fig. S3.

Table S2. Comparison of spin texture in nonmagnetic materials and anomalous Hall texture in altermagnets.

	Spin texture	anomalous Hall texture
Relationship	Spin-wave vector $\mathbf{s} - \mathbf{k}$	Anomalous Hall vector-Néel vector $\boldsymbol{\sigma}_H - \mathbf{n}$
Vector types	\mathbf{s} : axial vector \mathbf{k} : polar vector	$\boldsymbol{\sigma}_H$: axial vector \mathbf{n} : polar-like vector
Conditions of emergence	SOC effect, spatial inversion symmetry breaking	SOC effect, time-reversal symmetry breaking
Constraints of the independent variable	\mathbf{k} can be any arbitrary values	$ \mathbf{n} =1$
Constraints of the dependent variable	$ \mathbf{s} = \frac{\hbar}{2}$	$\boldsymbol{\sigma}_H$ can be any arbitrary values
Time-reversal operation	$\mathbf{s}(\mathbf{k}) = -\mathbf{s}(-\mathbf{k})$	$\boldsymbol{\sigma}_H(\mathbf{n}) = -\boldsymbol{\sigma}_H(-\mathbf{n})$

The comparison of spin texture and AHNTs is presented in Table S2. The spin \mathbf{s} and anomalous Hall conductivity $\boldsymbol{\sigma}_H$ axial vectors. Similar to moment \mathbf{k} , the Néel vector is a polar-like vector, because it switches its sign under the inversion symmetry (see Fig. 2 (a) of the main text). Due to the time-reversal symmetry, the spin texture satisfies $\mathbf{s}(\mathbf{k}) = -\mathbf{s}(-\mathbf{k})$ in nonmagnetic materials. A similar relation also exists in anomalous Hall texture: $\boldsymbol{\sigma}_H(\mathbf{n}) = -\boldsymbol{\sigma}_H(-\mathbf{n})$, due to the odd parity of $\boldsymbol{\sigma}_H$ with the time-reversal operation. In all, the anomalous Hall vector $\boldsymbol{\sigma}_H$ in the Néel vector space closely resembles the spin in the reciprocal moment space. This similarity can be attributed to the fact that both the spin-orbit coupling (SOC) field and the AHE vector $\boldsymbol{\sigma}_H$ are pseudovectors, and they are governed by similar (equivalent) point group symmetries. By drawing an analogy to the

spin texture, we can refer to the $\sigma_H - \mathbf{n}$ relation as the anomalous Hall texture in the Néel vector space.

Section IV. Completeness of $\sigma_H(\mathbf{n})$ relations in altermagnets

As mentioned above, we can transform the $\sigma_H - \mathbf{n}$ relations within the context of magnetic groups into a problem related to nonmagnetic space groups. It is important to note that in Eqs. (17) and (19), aside from the ± 1 sign, the remaining components are equivalent to the point group operations R acting on second- and fourth-order tensors. If we interpret the ± 1 arising from the exchange of magnetic atoms in these equations as the determinant of the point operation matrix R ($\det|R|$), we can see that $\mathbf{T}^{(2)}$ and $\mathbf{T}^{(4)}$ exhibit similarities to the second- and fourth-order axial tensor, respectively. Specifically, when $\{R|\mathbf{t}\}$ operations exchange magnetic atoms, we define the determinant of R as negative, and treat R as improper point operations IR (I is the inversion operation) for the axial tensors $\mathbf{T}^{(2)}$ and $\mathbf{T}^{(4)}$. Conversely, if the magnetic atoms are not exchanged under $\{R|\mathbf{t}\}$, we set $\det|R|=1$, and R acts as the proper point operations on $\mathbf{T}^{(2)}$ and $\mathbf{T}^{(4)}$.

Thus, solving all $\sigma_H(\mathbf{n})$ relationships is equivalent to exploring the behavior of second- and fourth-order axial tensors under the 32 crystallographic point groups. We can leverage group theory to simplify this exploration and investigate the completed $\sigma_H(\mathbf{n})$ relations in altermagnets. Specifically, the AHE tensors $\mathbf{T}^{(2)}$ exhibit similarities with general second-order axial tensors. In the context of the “extrinsic parameter” method, it suffices to utilize the nonmagnetic group, rather than the magnetic group, to investigate the symmetry constraints imposed on $\mathbf{T}^{(2)}$. Because the inversion symmetry prohibits the presence of axial tensor elements, only 21 non-centrosymmetric crystallographic point groups can accommodate nonzero second- and fourth-order axial tensors. We list all the equivalent symmetry-constrained axial tensors $\mathbf{T}^{(2)}$ as shown in Fig. S3, where the corresponding AHE textures are also listed. Among them, 11 chiral point groups (1, 2, 222, 4, 422, 3, 32, 6, 622, 23, and 432) lack improper symmetry operations with a determinant of $\det|R|=-1$. It means that there is no symmetry to exchange spin-opposite magnetic atoms in magnetic materials, resulting in uncompensated spin magnetic moments, therefore the cases where the equivalent constrained-symmetries are equivalent to chiral point groups are rule out in our study. From Fig. S3, we can see that the Rashba-like, Dresselhaus-like and pure cubic AHNTs can exist in altermagnetic materials, while the radical texture which is common in ferromagnetic is absent.

Non-centrosymmetric point group (PG)		
Polar non-chiral PGs	Non-Polar non-chiral PGs	Chiral PGs
$m: \begin{pmatrix} 0 & 0 & T_{13} \\ 0 & 0 & T_{23} \\ T_{31} & T_{32} & 0 \end{pmatrix}$ $2mm: \begin{pmatrix} 0 & T_{xy} & 0 \\ T_{yx} & 0 & 0 \\ 0 & 0 & 0 \end{pmatrix}$ Rashba & Dresselhaus	Dresselhaus texture $\bar{4}: \begin{pmatrix} T_{xx} & T_{xy} & 0 \\ T_{xy} & -T_{xx} & 0 \\ 0 & 0 & 0 \end{pmatrix}$ $\bar{4}2m: \begin{pmatrix} T_{xx} & 0 & 0 \\ 0 & -T_{xx} & 0 \\ 0 & 0 & 0 \end{pmatrix}$ $\bar{4}m2: \begin{pmatrix} 0 & T_{xy} & 0 \\ T_{yx} & 0 & 0 \\ 0 & 0 & 0 \end{pmatrix}$	$1: \begin{pmatrix} T_{xx} & T_{xy} & T_{xz} \\ T_{yx} & T_{yy} & T_{yz} \\ T_{zx} & T_{zy} & T_{zz} \end{pmatrix}$ $2: \begin{pmatrix} T_{xx} & T_{xy} & 0 \\ T_{yx} & T_{yy} & 0 \\ 0 & 0 & T_{zz} \end{pmatrix}$ No constrain
$\begin{matrix} 3m \\ 4mm \\ 6mm \end{matrix} : \begin{pmatrix} 0 & T_{xy} & 0 \\ -T_{xy} & 0 & 0 \\ 0 & 0 & 0 \end{pmatrix}$ Rashba texture	Pure cubic texture $\bar{6} : \begin{pmatrix} 0 & 0 & 0 \\ 0 & 0 & 0 \\ 0 & 0 & 0 \end{pmatrix}$ $\bar{6}m2 : \begin{pmatrix} 0 & 0 & 0 \\ 0 & 0 & 0 \\ 0 & 0 & 0 \end{pmatrix}$ $\bar{4}3m : \begin{pmatrix} 0 & 0 & 0 \\ 0 & 0 & 0 \\ 0 & 0 & 0 \end{pmatrix}$	$\begin{matrix} 3 \\ 4 \\ 6 \end{matrix} : \begin{pmatrix} T_{xx} & T_{xy} & 0 \\ -T_{xy} & T_{xx} & 0 \\ 0 & 0 & T_{zz} \end{pmatrix}$ Rashba & Radial texture $\begin{matrix} 23 \\ 432 \end{matrix} : \begin{pmatrix} T_{xx} & 0 & 0 \\ 0 & T_{xx} & 0 \\ 0 & 0 & T_{xx} \end{pmatrix}$ $\begin{matrix} 32 \\ 422 \\ 622 \end{matrix} : \begin{pmatrix} T_{xx} & 0 & 0 \\ 0 & T_{yy} & 0 \\ 0 & 0 & T_{zz} \end{pmatrix}$ Radial texture

Fig. S3 The equivalent point group symmetry constrained of $\mathbf{T}^{(2)}$ and corresponding AHE texture in 21 noncentrosymmetric point groups. The forms of $\mathbf{T}^{(2)}$ are equivalent to the $\mathcal{T}^{(2)}$ tensors in spin textures for all point groups. The equivalent chiral point groups are not allowed for AHNTs in altermagnets due to the uncompensated magnetic moments.

Based on these constraints, we identified 10 non-centrosymmetric and non-chiral point groups (m , $mm2$, $\bar{4}$, $4mm$, $\bar{4}2m$ ($\bar{4}m2$), $3m1$ ($31m$), $\bar{6}$, $6mm$, $\bar{6}m2$ ($\bar{6}2m$), and $\bar{4}3m$) to explore all possible cases of the $\sigma_H(\mathbf{n})$ relations in altermagnets. As summarized in Table S3, the $\sigma_H(\mathbf{n})$ relations exhibit the following characteristics:

1. There are no equal diagonal terms for $\mathbf{T}^{(2)}$ in all of the above point groups, which indicates that altermagnetic materials do not allow for radial AHNTs, such as $A(n_x, n_y, 0)$ or $A(n_x, n_y, n_z)$.
2. In the $\bar{6}$, $\bar{6}m2$ ($\bar{6}2m$), and $\bar{4}3m$ point groups, the existence of second-order axial tensors $\mathbf{T}^{(2)}$ is not allowed. Therefore, there is no first-order term for $\sigma_H(\mathbf{n})$, resulting in pure cubic AHNTs in altermagnets.
3. If the symmetry composed on σ_H is equivalent to the $3m$, $4mm$, or $6mm$, only the Rashba term $\sigma_H = A(n_y, -n_x, 0)$ exists for the first-order term in AHNTs.
4. The pure Dresselhaus AHNTs can only occur if the symmetry composed on σ_H identifies with the tetragonal group $\bar{4}2m$ ($\sigma_H = A(n_y, n_x, 0)$), $\bar{4}m2$ ($\sigma_H = A(n_x, -n_y, 0)$), or $\bar{4}$ ($\sigma_H = A(n_y, n_x, 0) + B(n_x, -n_y, 0)$).
5. Under the symmetry constraints equivalent to the monoclinic (m) or orthogonal ($mm2$) group, $\sigma_H(\mathbf{n})$ exhibits a mixed Rashba and Dresselhaus texture.

Table S3 All the possible $\sigma_H(\mathbf{n})$ relations, and corresponding AHNTs based on 10 non-centrosymmetric and non-chiral point groups.

Point group	Expressions	Independent elements	AHNTs
m (m⊥z)	$\sigma_H(\mathbf{n}) = \begin{pmatrix} T_{xz}n_z \\ T_{yz}n_z \\ T_{zx}n_x + T_{zy}n_y \end{pmatrix} + \begin{pmatrix} T_{xzz}n_z^3 + 3n_x^2T_{xxx}n_z + 6T_{xxyz}n_xn_y n_z + 3T_{xyyz}n_y^2n_z \\ T_{yzz}n_z^3 + 3n_y^2T_{yyy}n_z + 6n_xn_yT_{xyyz}n_z + 3T_{yzyz}n_z^2n_x \\ T_{zxx}n_x^3 + 3T_{zxyy}n_yn_x^2 + 3T_{zyyz}n_y^2n_x + 3n_z^2T_{zzzz}n_x + T_{zyyy}n_y^3 + 3T_{zyzz}n_yn_z^2 \end{pmatrix}$	1 st order: 4 3 rd order: 14	Mixed Rashba and Dresselhaus texture
mm2 (2//z)	$\sigma_H(\mathbf{n}) = \begin{pmatrix} T_{xy}n_y \\ T_{yx}n_x \\ 0 \end{pmatrix} + \begin{pmatrix} T_{xyyy}n_y^3 + 3T_{xxyy}n_x^2n_y + 3T_{xyzz}n_z^2n_y \\ T_{yxxx}n_x^3 + 3T_{yxyy}n_y^2n_x + 3T_{yzzz}n_z^2n_x \\ 6T_{zxyz}n_xn_y n_z \end{pmatrix}$	1 st order: 2 3 rd order: 7	Mixed Rashba and Dresselhaus texture
$\bar{4}$	$\sigma_H(\mathbf{n}) = \begin{pmatrix} T_{xx}n_x + T_{xy}n_y \\ T_{xy}n_x - T_{xx}n_y \\ 0 \end{pmatrix} + \begin{pmatrix} T_{xxxx}n_x^3 + 3T_{xxyy}n_yn_x^2 + 3T_{xyyy}n_y^2n_x + 3T_{xzzz}n_z^2n_x + T_{xyyy}n_y^3 + 3T_{xyzz}n_yn_z^2 \\ T_{xyyy}n_x^3 - 3T_{xxyy}n_yn_x^2 + 3T_{xyyy}n_y^2n_x + 3T_{xyzz}n_z^2n_x - T_{xxxx}n_x^3 - 3T_{xzzz}n_yn_z^2 \\ 3T_{zzxz}n_z^2n_x + 6T_{zzyz}n_yn_zn_x - 3T_{zzzz}n_y^2n_z \end{pmatrix}$	1 st order: 2 3 rd order: 8	Dresselhaus
4mm	$\sigma_H(\mathbf{n}) = \begin{pmatrix} T_{xy}n_y \\ -T_{xy}n_x \\ 0 \end{pmatrix} + \begin{pmatrix} T_{xyyy}n_y^3 + 3T_{xxyy}n_x^2n_y + 3T_{xyzz}n_z^2n_y \\ -T_{xyyy}n_x^3 - 3T_{xxyy}n_y^2n_x - 3T_{xyzz}n_z^2n_x \\ 0 \end{pmatrix}$	1 st order: 1 3 rd order: 3	Rashba
$\bar{4}2m$	$\sigma_H(\mathbf{n}) = \begin{pmatrix} T_{xx}n_x \\ -T_{xx}n_y \\ 0 \end{pmatrix} + \begin{pmatrix} T_{xxxx}n_x^3 + 3T_{xxyy}n_xn_y^2 + 3T_{xzzz}n_xn_z^2 \\ -3T_{xxyy}n_x^2n_y - T_{xxxx}n_y^3 - 3T_{xzzz}n_yn_z^2 \\ 3T_{zzxz}n_x^2n_z - 3T_{zzzz}n_y^2n_z \end{pmatrix}$	1 st order: 1 3 rd order: 4	Dresselhaus
$\bar{4}m2$	$\sigma_H(\mathbf{n}) = \begin{pmatrix} n_yT_{xy} \\ n_xT_{xy} \\ 0 \end{pmatrix} + \begin{pmatrix} T_{xyyy}n_y^3 + 3T_{xxyy}n_x^2n_y + 3T_{xyzz}n_z^2n_y \\ T_{xyyy}n_x^3 + 3T_{xxyy}n_y^2n_x + 3T_{xyzz}n_z^2n_x \\ 6T_{zxyz}n_xn_y n_z \end{pmatrix}$	1 st order: 1 3 rd order: 4	Dresselhaus
3m1	$\sigma_H(\mathbf{n}) = \begin{pmatrix} n_yT_{xy} \\ -n_xT_{xy} \\ 0 \end{pmatrix} + \begin{pmatrix} 3T_{xxyy}n_y^3 - 3T_{xzzz}n_z^2n_y + 3T_{xxyy}n_x^2n_y + 3T_{xyzz}n_z^2n_y + 3T_{xzzz}n_x^2n_z \\ -3T_{xxyy}n_x^3 - 3T_{xxyy}n_y^2n_x - 6T_{xzzz}n_yn_zn_x - 3T_{xyzz}n_z^2n_x \\ T_{zzzz}n_x^3 - 3T_{zzzz}n_xn_y^2 \end{pmatrix}$	1 st order: 1 3 rd order: 4	Rashba
31m	$\sigma_H(\mathbf{n}) = \begin{pmatrix} n_yT_{xy} \\ -n_xT_{xy} \\ 0 \end{pmatrix} + \begin{pmatrix} 3T_{xxyy}n_y^3 + 3T_{xxyy}n_x^2n_y + 6T_{xxyz}n_xn_zn_y + 3T_{xyzz}n_z^2n_y \\ -3T_{xxyy}n_x^3 + 3T_{xxyz}n_zn_x^2 - 3T_{xxyy}n_y^2n_x - 3T_{xyzz}n_z^2n_x - 3T_{xxyz}n_y^2n_z \\ 3T_{zxyy}n_x^2n_y - T_{zxyy}n_y^3 \end{pmatrix}$	1 st order: 1 3 rd order: 4	Rashba
$\bar{6}$	$\sigma_H(\mathbf{n}) = \begin{pmatrix} 0 \\ 0 \\ 0 \end{pmatrix} + \begin{pmatrix} 3T_{xzzz}n_zn_x^2 + 6T_{xxyz}n_yn_zn_x - 3T_{xzzz}n_y^2n_z \\ 3T_{xxyz}n_zn_x^2 - 6T_{xzzz}n_yn_zn_x - 3T_{xxyz}n_y^2n_z \\ T_{zzzz}n_x^3 + 3T_{zxyy}n_yn_x^2 - 3T_{zzzz}n_y^2n_x - T_{zxyy}n_y^3 \end{pmatrix}$	1 st order: 0 3 rd order: 4	Pure cubic texture
6mm	$\sigma_H(\mathbf{n}) = \begin{pmatrix} T_{xy}n_y \\ -T_{xy}n_x \\ 0 \end{pmatrix} + \begin{pmatrix} 3T_{xxyy}n_x^2n_y + 3T_{xxyy}n_y^3 + 3T_{xyzz}n_yn_z^2 \\ -3T_{xxyy}n_xn_y^2 - 3T_{xxyy}n_x^3 - 3T_{xyzz}n_xn_z^2 \\ 0 \end{pmatrix}$	1 st order: 1 3 rd order: 2	Rashba

$\bar{6}m2$	$\boldsymbol{\sigma}_H(\mathbf{n}) = \begin{pmatrix} 0 \\ 0 \\ 0 \end{pmatrix} + \begin{pmatrix} 3T_{\text{xxxz}}n_x^2n_z - 3T_{\text{xxxz}}n_y^2n_z \\ -6T_{\text{xxxz}}n_xn_yn_z \\ T_{\text{zxxx}}n_x^3 - 3T_{\text{zxxx}}n_xn_y^2 \end{pmatrix}$	1 st order: 0 3 rd order: 2	Pure cubic texture
$\bar{6}2m$	$\boldsymbol{\sigma}_H(\mathbf{n}) = \begin{pmatrix} 0 \\ 0 \\ 0 \end{pmatrix} + \begin{pmatrix} 6T_{\text{xyyz}}n_xn_yn_z \\ 3T_{\text{xyyz}}n_x^2n_z - 3T_{\text{xyyz}}n_y^2n_z \\ 3T_{\text{zxyy}}n_x^2n_y - T_{\text{zxyy}}n_y^3 \end{pmatrix}$	1 st order: 0 3 rd order: 2	Pure cubic texture
$\bar{4}3m$	$\boldsymbol{\sigma}_H(\mathbf{n}) = \begin{pmatrix} 0 \\ 0 \\ 0 \end{pmatrix} + \begin{pmatrix} 3T_{\text{xyyy}}n_xn_y^2 - 3T_{\text{xyyy}}n_xn_z^2 \\ 3T_{\text{xyyy}}n_yn_z^2 - 3T_{\text{xyyy}}n_x^2n_y \\ 3T_{\text{xyyy}}n_x^2n_z - 3T_{\text{xyyy}}n_y^2n_z \end{pmatrix}$	1 st order: 0 3 rd order: 1	Pure cubic texture

We also identified the groups that frequently occur in altermagnetic materials [8-11]: $P2_1/n$ (14), $C2/c$ (15), $Cmcm$ (63), $Pnma$ (62), $P4_2/mnm$ (136), $I4/mcm$ (140), $R\bar{3}c$ (167), and $P6_3/mmc$ (194), all of which fall into the aforementioned category. Besides, with the help of Table S3, we can quickly identify the AHE texture for real altermagnetic materials, because it simplifies and streamlines the symmetry analysis. For example, if $\{R|\mathbf{t}\}$ operation exchanges magnetic atoms, we define its determinant as negative, and treat R as improper point operations IR (I is the inversion symmetry) for the axial tensors $\mathbf{T}^{(2)}$ and $\mathbf{T}^{(4)}$. Conversely, if the magnetic atoms are not exchanged under $\{R|\mathbf{t}\}$, we set $\det|R|=1$, allowing R to act as the proper point operations on $\mathbf{T}^{(2)}$ and $\mathbf{T}^{(4)}$. From there, we can identify the equivalent point groups and corresponding $\boldsymbol{\sigma}_H(\mathbf{n})$ relations in Table S3. Specific examples are provided in Sec. VI.

Section V. Projection to real sphere harmonics and multipoles

Analogous to the Berry curvature multipoles in reciprocal moment space [12-14] and the magnetic multipoles in real space [15-17], Eq. (21) can be interpreted as the AHE multipoles within the Néel vector space. Subsequently, we proceed to project $\boldsymbol{\sigma}_H$ into the basis of Néel vector multipoles.

The linear term of $\boldsymbol{\sigma}_H$ on \mathbf{n} has three independent elements in Eq. (10), namely n_x , n_y , n_z . Besides, the cubic term of $\boldsymbol{\sigma}_H$ has the commutative symmetry as stated in Eq. (20), resulting in 10 independent Taylor expansion terms, namely, n_x^3 , n_y^3 , n_z^3 , $n_xn_yn_z$, $n_x^2n_z$, $n_y^2n_z$, $n_xn_z^2$, $n_yn_z^2$, $n_xn_y^2$ and $n_x^2n_y$. Additionally, \mathbf{n} is a unit vector ($|\mathbf{n}|=1$), i.e., $n_x^2 + n_y^2 + n_z^2 = 1$. This constraint reduces the independent cubic terms to 7, which is significant as they coincide with the f spherical harmonics with angular momentum $l=3$. Consequently,

it becomes feasible to project the anomalous Hall vector $\boldsymbol{\sigma}_H$ onto the basis of real spherical harmonics with p and f orbitals. The three real p spherical harmonics for $\ell=1$ are:

$$\begin{cases} p_z = \sqrt{\frac{3}{4\pi}} \cos \theta, \\ p_x = \sqrt{\frac{3}{4\pi}} \sin \theta \cos \varphi, \\ p_y = \sqrt{\frac{3}{4\pi}} \sin \theta \sin \varphi, \end{cases} \quad (27)$$

where θ is the polar angle, and φ is the azimuthal angle. The seven real f spherical harmonics with $\ell=3$ are:

$$\begin{cases} f_{z^3} = Y_3^0 = \frac{\sqrt{7}}{4\sqrt{\pi}} (5 \cos^3 \theta - 3 \cos \theta), \\ f_{xz^2} = \frac{1}{\sqrt{2}} (Y_3^{-1} - Y_3^1) = \frac{\sqrt{21}}{4\sqrt{2\pi}} (5 \cos^2 \theta - 1) \sin \theta \cos \varphi, \\ f_{yz^2} = \frac{i}{\sqrt{2}} (Y_3^{-1} + Y_3^1) = \frac{\sqrt{21}}{4\sqrt{2\pi}} (5 \cos^2 \theta - 1) \sin \theta \sin \varphi, \\ f_{z(x^2-y^2)} = \frac{1}{\sqrt{2}} (Y_3^2 + Y_3^{-2}) = \frac{\sqrt{105}}{4\sqrt{\pi}} \sin^2 \theta \cos \theta \cos 2\varphi, \\ f_{xyz} = \frac{i}{\sqrt{2}} (Y_3^{-2} - Y_3^2) = \frac{\sqrt{105}}{4\sqrt{\pi}} \sin^2 \theta \cos \theta \sin 2\varphi, \\ f_{x(x^2-3y^2)} = \frac{1}{\sqrt{2}} (Y_3^{-3} - Y_3^3) = \frac{\sqrt{35}}{4\sqrt{2\pi}} \sin^3 \theta (\cos^2 \varphi - 3 \sin^2 \varphi) \cos \varphi, \\ f_{y(3x^2-y^2)} = \frac{i}{\sqrt{2}} (Y_3^{-3} + Y_3^3) = \frac{\sqrt{35}}{4\sqrt{2\pi}} \sin^3 \theta (3 \cos^2 \varphi - \sin^2 \varphi) \sin \varphi. \end{cases} \quad (28)$$

The multipoles with p and f configurations are shown in Fig. S4. For an arbitrary real spherical harmonic ϕ_i in Eq. (27) and Eq. (28), it obeys:

$$\int_0^{2\pi} d\varphi \int_0^\pi \phi_i \phi_j \sin \theta d\theta = \delta_{ij}, \quad (29)$$

where δ_{ij} is the Kronecker delta function. The real spherical harmonics are orthogonal and normalized. Thus, $\{\phi_i\} = \{p_z, p_x, p_y, f_{z^3}, f_{xz^2}, f_{yz^2}, f_{z(x^2-y^2)}, f_{xyz}, f_{x(x^2-3y^2)}, f_{y(3x^2-y^2)}\}$ forms a complete and independent basis set in the multipole space.

We utilize the relations $n_x = \sin \theta \cos \varphi$, $n_y = \sin \theta \sin \varphi$, and $n_z = \cos \theta$ to convert $\boldsymbol{\sigma}_H$ from Cartesian coordinates in Eq. (21) to spherical coordinates. The expanded coefficient of $\boldsymbol{\sigma}_H$ within the basis ϕ_j is:

$$\zeta_{ij} = \int_0^{2\pi} d\varphi \int_0^\pi \sigma_i \phi_j \sin \theta d\theta. \quad (30)$$

The coefficients of the p sphere harmonics function represent the dipoles in Néel vector space, and the f sphere harmonics function to the octupoles. Finally, the anomalous Hall vector $\boldsymbol{\sigma}_H$ can be expressed as the multipoles as follows:

$$\sigma_i = \sum_j \zeta_{ij} \phi_j. \quad (31)$$

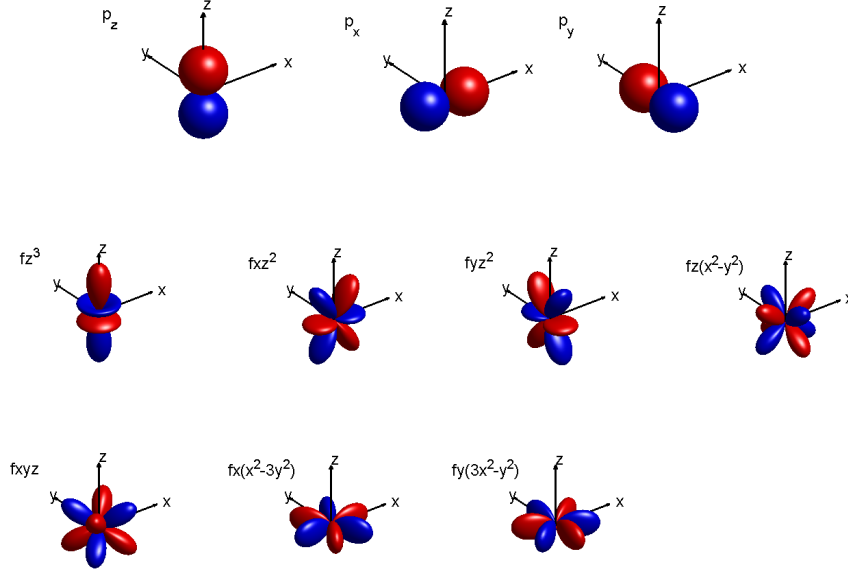


Fig. S4. Real spherical harmonics of p and f orbitals.

The multipoles of $\boldsymbol{\sigma}_H$ in the Néel vector space reflect the complexity of the spin-orbits coupling (SOC) effect [3]. For example, the spin-conserving part contributes to the dipole at the first order, whereas the spin-flip segment contributes at the second order. The scaling of the octupole varies with the nature of the SOC effect, following λ^3 for the spin-conserving part and λ^4 for the spin-flip portion.

Section VI. Anomalous-Hall Néel textures of typical altermagnets

V.A Rutile-type altermagnetic materials

The parent space group of rutile-type altermagnets is $P4_2/mnm$ (No. 136). This space group encompasses 16 fundamental operations, and 4_2 , g_x , g_y , and m_z serve as the generation operations. The transformation of anomalous Hall vector $\boldsymbol{\sigma}_H$ and Néel vector \mathbf{n} under these operations are given in Table S4, and the equivalent point operations are also listed. According to equivalent point operations, the constraints on $\mathbf{T}^{(2)}$ and $\mathbf{T}^{(4)}$ are equivalent to those of points group $\overline{4}m2$.

Table S4. Transformations of $\boldsymbol{\sigma}_H$ and \mathbf{n} of rutile-type altermagnets with the space group of $P4_2/mnm$. σ_i ($i=x, y$ or z) is the anomalous Hall conductivity along the i direction.

$\{R \mathbf{t}\}$	$(\sigma_x, \sigma_y, \sigma_z)$	Switch opposite magnetic atoms or not?	(n_x, n_y, n_z)	Equivalent point operation
g_x	$(\sigma_x, -\sigma_y, -\sigma_z)$	yes	$(-n_x, n_y, n_z)$	m_x
g_y	$(-\sigma_x, \sigma_y, -\sigma_z)$	yes	$(n_x, -n_y, n_z)$	m_y
m_z	$(-\sigma_x, -\sigma_y, \sigma_z)$	no	$(-n_x, -n_y, n_z)$	2_z
4_2	$(\sigma_y, -\sigma_x, \sigma_z)$	yes	$(-n_y, n_x, -n_z)$	$\bar{4}$

Based on Table S4 and the AHE-texture code, we can determine $\boldsymbol{\sigma}_H$ within first-order and third-order terms of \mathbf{n} as follows:

$$\begin{aligned} \boldsymbol{\sigma}_H(\mathbf{n}) &= (An_y, An_x, 0) + (an_x^2n_y + bn_y^3 + cn_y n_z^2, bn_x^3 + an_x n_y^2 + cn_x n_z^2, dn_x n_y n_z) \\ &= \left(\alpha p_y - \beta f_{yz^2} + \gamma f_{y(3x^2-y^2)}, \alpha p_x - \beta f_{xz^2} - \gamma f_{x(3x^2-y^2)}, \lambda f_{xyz} \right), \end{aligned} \quad (32)$$

where $\alpha = \frac{2}{5}\sqrt{\frac{\pi}{3}}(5A + a + 3b + c)$ is the AHE dipole coefficient in the Néel vector space, $\beta = \frac{1}{5}\sqrt{\frac{2\pi}{21}}(a + 3b - 4c)$, $\gamma = \sqrt{\frac{2\pi}{35}}(a - b)$ and $\lambda = 2d\sqrt{\frac{\pi}{105}}$ are the AHE octupole coefficients in Néel vector space. This result is constant with that in Table S3.

V.B Calcite-type altermagnets

Calcite-type altermagnets have the $R\bar{3}c$ (No. 167) space group symmetry. The transformation of $\boldsymbol{\sigma}_H$ and \mathbf{n} under symmetry operations are given in Table S5, and the equivalent point operations are also listed. According to equivalent point operations, the constraints on $\mathbf{T}^{(2)}$ and $\mathbf{T}^{(4)}$ are equivalent to those of points group $3m1$.

Based on the extrinsic parameter method, the symmetry-constrained $\boldsymbol{\sigma}_H$ is:

$$\boldsymbol{\sigma}_H(\mathbf{n}) = \begin{pmatrix} T_{Xy} n_y \\ -T_{Xy} n_x \\ 0 \end{pmatrix} + \begin{pmatrix} 3T_{Xxy}(n_x^2 + n_y^2)n_y + 3T_{Xyz}(n_x^2 - n_y^2)n_z + 3T_{Xyz}n_y n_z^2 \\ -3T_{Xxy}(n_x^2 + n_y^2)n_x - 6T_{Xyz}n_x n_y n_z - 3T_{Xyz}n_x n_z^2 \\ T_{Zxy}n_x(n_x^2 - 3n_y^2) \end{pmatrix}, \quad (33)$$

where T_{Xy} , T_{Xxy} , T_{Xxz} , T_{Xyz} , T_{Zxx} are undetermined coefficients. This result is constant with that in Table S3.

Eq. (33) can be rewritten as the following multipoles:

$$\sigma_x = \frac{2}{5}\sqrt{\frac{\pi}{3}}(5T_{Xy} + 12T_{Xxy} + 3T_{Xyz})p_y + 4\sqrt{\frac{3\pi}{35}}T_{Xxz}f_{z(x^2-y^2)} - \frac{4}{5}\sqrt{\frac{6\pi}{7}}(T_{Xxy} - T_{Xyz})f_{yz^2}, \quad (34)$$

$$\sigma_y = -\frac{2}{5}\sqrt{\frac{\pi}{3}}(5T_{Xy} + 12T_{Xxy} + 3T_{Xyz})p_x - 4\sqrt{\frac{3\pi}{35}}T_{Xxz}f_{xyz} + \frac{4}{5}\sqrt{\frac{6\pi}{7}}(T_{Xxy} - T_{Xyz})f_{xz^2}, \quad (35)$$

$$\sigma_z = 4\sqrt{\frac{2\pi}{35}}T_{\text{Zxxx}}f_x(x^2-3y^2). \quad (36)$$

Since the coefficients of the first-order terms of σ_x and σ_y are opposite, this results in a Rashba-like AHNTs.

Table S5. Transformations of $\boldsymbol{\sigma}_H$ and \mathbf{n} of calcite-type altermagnets with space group $R\bar{3}c$ (No. 167).

$\{R \mathbf{t}\}$	$(\sigma_x, \sigma_y, \sigma_z)$	Switch opposite magnetic atoms or not?	(n_x, n_y, n_z)	Equivalent point operation
g_x	$(\sigma_x, -\sigma_y, -\sigma_z)$	yes	$(-n_x, n_y, n_z)$	m_x
3	$\left(-\frac{\sigma_x}{2} + \frac{\sqrt{3}}{2}\sigma_y, -\frac{\sqrt{3}}{2}\sigma_x - \frac{1}{2}\sigma_y, \sigma_z\right)$	no	$\left(-\frac{n_x}{2} + \frac{\sqrt{3}}{2}n_y, -\frac{\sqrt{3}}{2}n_x - \frac{1}{2}n_y, n_z\right)$	3
$\bar{1}$	$(\sigma_x, \sigma_y, \sigma_z)$	no	(n_x, n_y, n_z)	1

V.C NiAs-type altermagnetic materials

The parent space group of NiAs-type altermagnets is $P6_3/mmc$ (No. 194). It has 24 basic operations, and 6_3 , m_x , g_y , and m_z are the generation operations. The transformation manners of the anomalous Hall vector $\boldsymbol{\sigma}_H$ and the Néel vector \mathbf{n} under these operations are outlined in Table S6, and the equivalent point operations are also listed. According to equivalent point operations, the constraints on $\mathbf{T}^{(2)}$ and $\mathbf{T}^{(4)}$ are equivalent to those of points group $\bar{6}2m$.

Table S6. Transformations of $\boldsymbol{\sigma}_H$ and \mathbf{n} in NiAs-type altermagnets with space group $P6_3/mmc$.

$\{R \mathbf{t}\}$	$(\sigma_x, \sigma_y, \sigma_z)$	Switch opposite magnetic atoms or not?	(n_x, n_y, n_z)	Equivalent point operation
m_x	$(\sigma_x, -\sigma_y, -\sigma_z)$	no	$(n_x, -n_y, -n_z)$	2_x
g_y	$(-\sigma_x, \sigma_y, -\sigma_z)$	yes	$(n_x, -n_y, n_z)$	m_y
m_z	$(-\sigma_x, -\sigma_y, \sigma_z)$	yes	$(n_x, n_y, -n_z)$	m_z
6_3	$\left(\frac{\sigma_x}{2} + \frac{\sqrt{3}}{2}\sigma_y, -\frac{\sqrt{3}}{2}\sigma_x + \frac{1}{2}\sigma_y, \sigma_z\right)$	yes	$\left(-\frac{n_x}{2} - \frac{\sqrt{3}}{2}n_y, \frac{\sqrt{3}}{2}n_x - \frac{1}{2}n_y, -n_z\right)$	$\bar{6}$

Based on the above characters, we can drive $\boldsymbol{\sigma}_H$ within Néel vector \mathbf{n} polynomials up to third-order terms with the help of AHE-texture code. $\boldsymbol{\sigma}_H$ can be written as:

$$\begin{aligned} \boldsymbol{\sigma}_H(\mathbf{n}) &= \left[2an_x n_y n_z, a(n_x^2 - n_y^2)n_z, c(3n_x^2 n_y - n_y^3) \right] \\ &= \left[a\sqrt{\frac{\pi}{105}}f_{xyz}, a\sqrt{\frac{\pi}{105}}f_{(x^2-y^2)z}, c\sqrt{\frac{2\pi}{35}}f_{(3x^2-y^2)y} \right], \end{aligned} \quad (37)$$

where the linear order terms are forbidden by symmetry. This result is constant with that in Table S3.

Section VII. Effective TB models and calculation method

We use the s -orbitals of the magnetic atoms to construct the effective tight-binding (TB) Hamiltonians. First, we utilize the MagneticTB [18] program to obtain symmetry-constrained effective Hamiltonians with spin-orbit coupling (SOC) effect but without magnetism. Under the symmetry operation $\{R|\mathbf{t}\}$, the TB Hamiltonian satisfies:

$$P(\{R|\mathbf{t}\})^{-1} H(\mathbf{k}) P(\{R|\mathbf{t}\}) = H^*(-R^{-1}\mathbf{k}), \quad (38)$$

where the $P(\{R|\mathbf{t}\})$ is the symmetry operation matrix under the orbital bases. Finally, we add the on-site magnetic exchange interactions, as follows:

$$H_{mag} = (-1)^i \sum_i \mathbf{m} \cdot \boldsymbol{\sigma} c_i^+ c_i, \quad (39)$$

where i denotes the site index of magnetic atoms, $\boldsymbol{\sigma}$ represents the Pauli matrices, and $\mathbf{m} = m(\sin \theta \cos \varphi, \sin \theta \sin \varphi, \cos \theta)$ is the magnetic moments. Eq. (39) ensures that the magnetic moments of the two sublattices of altermagnets are anti-parallel all the way, i.e., there is no net magnetic moment when the Néel vector changes.

According to Kubo-Greenwood theory, we compute the coefficients for the AHE and the magneto-optical effects as follows:

$$\sigma_\gamma(\omega) = \frac{ie^2\hbar}{N_k \Omega_c} \varepsilon_{\alpha\beta\gamma} \sum_k \sum_{n,m} \frac{f_{mk} - f_{nk}}{\varepsilon_{mk} - \varepsilon_{nk}} \frac{\langle \psi_{nk} | v_\alpha | \psi_{mk} \rangle \langle \psi_{mk} | v_\beta | \psi_{nk} \rangle}{\varepsilon_{mk} - \varepsilon_{nk} - (\hbar\omega + i\eta)}, \quad (40)$$

where ω is the frequency of light, $\varepsilon_{\alpha\beta\gamma}$ is the Levi-Civita symbol. The anomalous Hall conductivity can be obtained when $\omega = 0$. Within the effective TB Hamiltonians, we use our own WRFP program to calculate the AHE and magnetic-optical coefficients.

VI.A Rutile-type altermagnetic materials

A rutile-type altermagnetic material has two magnetic atoms in A (0, 0, 0) and B (1/2, 1/2, 1/2), respectively. The effective TB Hamiltonian without magnetism under the basis of $\{A \uparrow, A \downarrow, B \uparrow, B \downarrow\}$ is:

$$H = \begin{bmatrix} 0 & 0 & H_{13} & H_{14} \\ 0 & 0 & -H_{14}^* & H_{13} \\ \dagger & \dagger & 0 & 0 \\ \dagger & \dagger & 0 & 0 \end{bmatrix}, \quad (41)$$

where

$$H_{13} = t \sum_{ij} c_i^+ c_j = 8t \cos\left(\frac{k_x}{2}\right) \cos\left(\frac{k_y}{2}\right) \cos\left(\frac{k_z}{2}\right), \quad (42)$$

is the hopping of two magnetic atoms, and

$$H_{14} = (4 + 4i)\lambda \left(\sin \left[\frac{k_x - k_y}{2} \right] + i \sin \left[\frac{k_x + k_y}{2} \right] \right) \sin \left(\frac{k_z}{2} \right), \quad (43)$$

is the SOC coupling term. This effective model is consistent with Refs. [19,20]. The band structures without the SOC effect are shown in Fig. S5(a). Whereafter, we incorporate the antiferromagnetic exchange interaction term using Eq. (39). The magnetism induces the band splitting, as shown in Fig. S5(b). The flat band at the X-S-Y arises from the fact that Eq. (41) model is too simplistic, leading to $H_{13} = 0$ and $H_{14} = 0$ at these paths. The AHE conductivities of the main text are adopted at -0.61 eV.

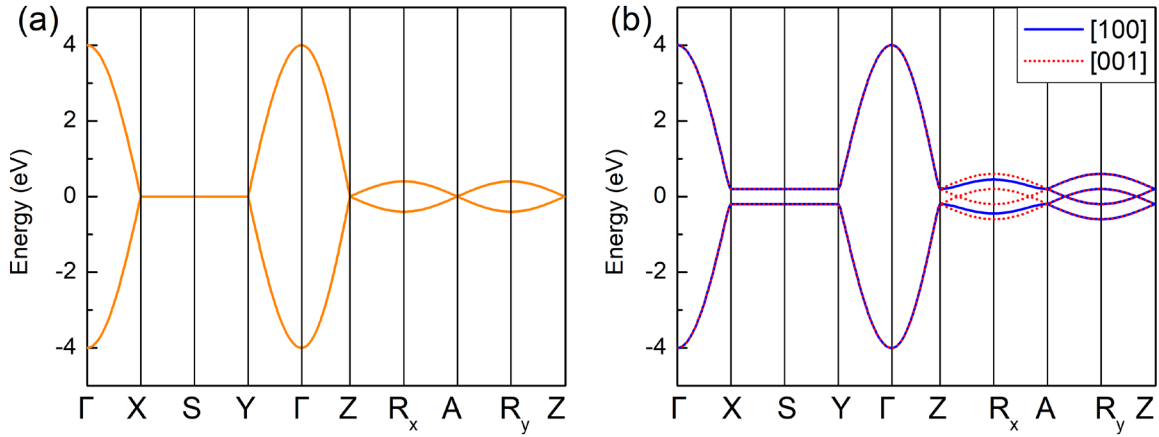


Fig. S5. Bands structures of effective TB model in Eq. (41) (a) without and (b) with magnetization. $t=0.5$ eV, $\lambda=0.05$ eV and $m=0.2$ eV. The vectors in (b) denote the Néel vectors.

VI.B Calcite-type altermagnetic materials

The primitive cell of calcite-type altermagnets with $R\bar{3}c$ space group is

$$\begin{cases} \mathbf{a}_1 = \frac{a}{2}\mathbf{i} + \frac{\sqrt{3}a}{6}\mathbf{j} + \frac{c}{3}\mathbf{k}, \\ \mathbf{a}_2 = -\frac{a}{2}\mathbf{i} + \frac{\sqrt{3}a}{6}\mathbf{j} + \frac{c}{3}\mathbf{k}, \\ \mathbf{a}_3 = -\frac{\sqrt{3}}{3}a\mathbf{j} + \frac{c}{3}\mathbf{k}, \end{cases} \quad (44)$$

where a and c are the lattice constants in the hexagonal cell. There are two magnetic atoms in each primitive cell, occupied at A (0, 0, 0) and B (1/2, 1/2, 1/2), respectively. The effective TB Hamiltonian without magnetism considering the second-nearest neighbor terms (A-B, A-A) is:

$$H = \begin{bmatrix} 0 & 0 & H_{13} & H_{14} \\ 0 & 0 & -H_{14}^* & H_{13} \\ \dagger & \dagger & 0 & 0 \\ \dagger & \dagger & 0 & 0 \end{bmatrix}, \quad (45)$$

where

$$H_{13} = 2(r_3 + ir_1) \left[2 \cos\left(\frac{k_x}{2}\right) \cos\left(\frac{k_y - k_z}{2}\right) + \cos\left(\frac{1}{2}(k_x - k_y - k_z)\right) \right] + 2(t_2 + it_1) \cos\left(\frac{1}{2}(k_x + k_y + k_z)\right), \quad (46)$$

and

$$H_{14} = 8r_2 \cos\left[\frac{k_z}{2}\right] \sin\left[\frac{k_x}{2}\right] \sin\left[\frac{k_y}{2}\right] + 4ir_2 \left(\sqrt{3} \sin\left[\frac{k_x - k_y}{2}\right] + i \sin\left[\frac{k_x + k_y}{2}\right] \right) \sin\left[\frac{k_z}{2}\right]. \quad (47)$$

The band structures are shown in Fig. S6. The AHE conductivities of the main text are adopted at -2.86 eV.

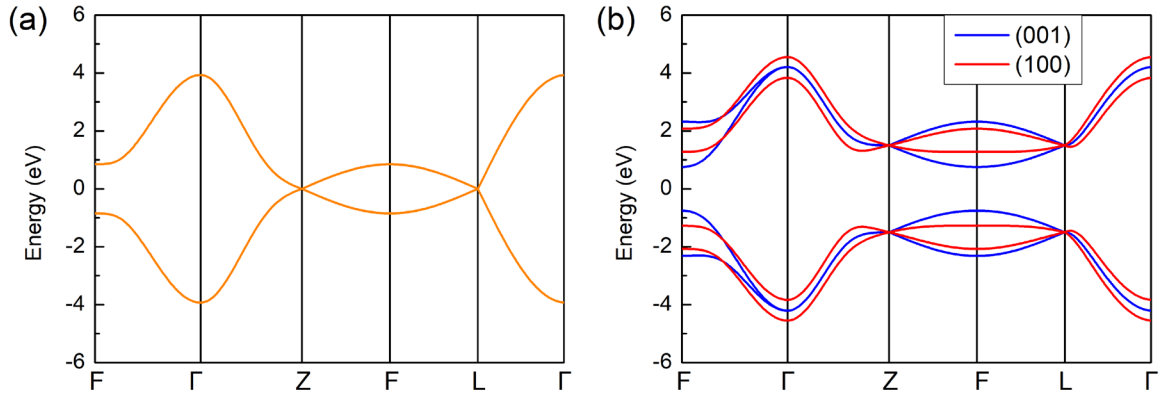


Fig. S6. Band structure of effective TB model in Eq. (45) (a) without and (b) with magnetization. $t_1 = 0.05$ eV, $t_2 = 0.4$ eV, $r_1 = 0.15$ eV, $r_2 = 0.1$ eV, $r_3 = 0.5$ eV and $m = 1.5$ eV. The vectors in (b) denote the Néel vectors.

VI.C NiAs-type altermagnetic materials

There are two magnetic atoms in each unit cell for the NiAs-type altermagnetic material, located at A (0, 0, 0) and B (0, 0, 1/2), respectively. The TB Hamiltonian without magnetism is:

$$H = \begin{bmatrix} H_{11} & 0 & H_{13} & H_{14} \\ 0 & H_{11} & -H_{14}^* & H_{13} \\ \dagger & \dagger & H_{11} & 0 \\ \dagger & \dagger & 0 & H_{11} \end{bmatrix}, \quad (48)$$

where

$$H_{11} = 2t_2 \left[\cos(k_x) + \cos(k_y) + \cos(k_x + k_y) \right] \quad (49)$$

is the hopping of six in-plane next-nearest neighbors, and

$$H_{13} = 2 \left[t_1 + 2t_3 \left(\cos(k_x) + \cos(k_y) + \cos(k_x + k_y) \right) \right] \cos\left(\frac{k_z}{2}\right) - 4i\lambda_1 \left[\sin(k_x) + \sin(k_y) - \sin(k_x + k_y) \right] \sin\left(\frac{k_z}{2}\right), \quad (50)$$

where t_1 is the nearest neighbor hopping, t_3 is the third-nearest neighbor hopping, and λ_1 is the SOC strength. H_{14} represents the SOC effect between different sublattices, and its expression is:

$$H_{14} = \frac{4}{3} \lambda_2 \left[-2i\sqrt{3} \cos(k_x) + i(3i + \sqrt{3}) \cos(k_y) + (3 + i\sqrt{3}) \cos(k_x + k_y) \right] \cos\left(\frac{k_z}{2}\right). \quad (51)$$

Finally, we incorporate the antiferromagnetic exchange interaction term using Eq. (39). The calculated energy bands are shown in Fig. S7. The anomalous Hall conductivity of the main text is adopted at -3 eV.

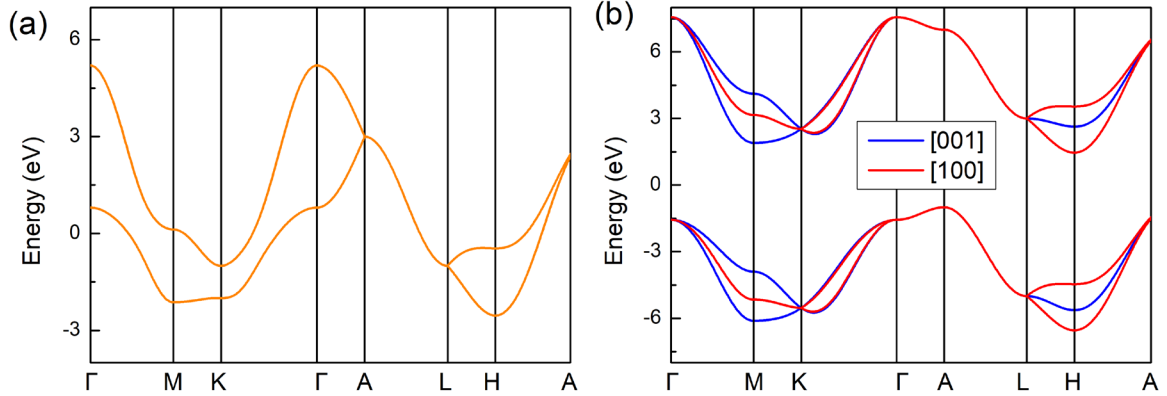


Fig. S7. Band structures of NiAs-type crystal with effective TB model in Eq. (48) (a) without and (b) with magnetization. $t_1=0.2$ eV, $t_2=0.5$ eV, $t_3=0.15$ eV, $\lambda_1=-0.1$ eV, $\lambda_2=0.12$ eV, $m=4.0$ eV. The vectors in (b) denote the Néel vectors.

Section VIII. AHNTs of perovskite-type altermagnetic materials

The perovskite-type altermagnetic materials represent a broad class of antiferromagnetic materials in the formula of ABO_3 , belonging to the space group Pnma (No. 62). An octahedron formed by six oxygen atoms surrounds each magnetic atom B, with non-magnetic A atoms situated at the center of these octahedra, as shown in Fig. S8(a). Typically, the magnetic atoms B occupy the 4b Wyckoff positions at $(1/2, 0, 0)$, $(0, 1/2, 1/2)$, $(1/2, 1/2, 0)$, and $(0, 0, 1/2)$. Consequently, there are 3 ($C_4^2 C_2^2 / A_2^2 = 3$) kinds of collinear antiferromagnetic configurations, indicating by A-type (e.g., LaMnO_3 , PrMnO_3 ,

NdMnO₃), C-type (e.g., CaCrO₃ [21], ScCrO₃), and G-type (e.g., NaOsO₃, LaCrO₃, TbCrO₃, NdFeO₃, TbFeO₃, etc.), as illustrated in Fig. S8(b).

The effective TB Hamiltonian without magnetism is given by:

$$H = \begin{pmatrix} 0 & 0 & H_{13} & H_{14} & H_{15} & H_{16} & H_{17} & H_{18} \\ 0 & 0 & -H_{14}^* & H_{13}^* & -H_{16}^* & H_{15}^* & -H_{18}^* & H_{17}^* \\ \dagger & \dagger & 0 & 0 & H_{17} & -H_{18}^* & H_{15}^* & -H_{16}^* \\ \dagger & \dagger & 0 & 0 & 0 & 0 & H_{16} & H_{15} \\ \dagger & \dagger & \dagger & \dagger & 0 & 0 & H_{57} & H_{58} \\ \dagger & \dagger & \dagger & \dagger & \dagger & \dagger & -H_{58}^* & H_{57}^* \\ \dagger & \dagger & \dagger & \dagger & \dagger & \dagger & 0 & 0 \\ \dagger & \dagger & \dagger & \dagger & \dagger & \dagger & 0 & 0 \end{pmatrix}, \quad (52)$$

where

$$H_{13} = 4 \cos\left(\frac{k_x}{2}\right) \left[(-is_2 + s_6) \cos\left(\frac{k_y - k_z}{2}\right) + (is_4 + s_8) \cos\left(\frac{k_y + k_z}{2}\right) \right], \quad (53)$$

where s_6 and s_8 are the hopping parameters, while s_2 and s_4 are the SOC coefficients. H_{14} represents the spin-orbit coupling between the $(1/2, 0, 0)$ and $(0, 1/2, 1/2)$ atoms:

$$H_{14} = 2 \left(\begin{aligned} & (is_3 + s_7) \cos\left[\frac{1}{2}(k_x - k_y - k_z)\right] + (-is_1 + s_5) \cos\left[\frac{1}{2}(k_x + k_y - k_z)\right] \\ & + (is_1 + s_5) \cos\left[\frac{1}{2}(k_x - k_y + k_z)\right] + (-is_3 + s_7) \cos\left[\frac{1}{2}(k_x + k_y + k_z)\right] \end{aligned} \right). \quad (54)$$

The hopping between $(\frac{1}{2}, 0, 0)$ and $(\frac{1}{2}, \frac{1}{2}, 0)$ is:

$$H_{15} = 2(it_2 + t_3) \cos\left(\frac{k_y}{2}\right), \quad (55)$$

$$H_{16} = -2it_1 \cos\left(\frac{k_y}{2}\right). \quad (56)$$

The hopping between $(\frac{1}{2}, 0, 0)$ and $(0, 0, \frac{1}{2})$ is:

$$H_{17} = 4r_4 \cos\left(\frac{k_x}{2}\right) \cos\left(\frac{k_z}{2}\right) + 4ir_2 \sin\left(\frac{k_x}{2}\right) \sin\left(\frac{k_z}{2}\right), \quad (57)$$

$$H_{18} = 4i(r_1 + ir_3) \cos\left(\frac{k_x}{2}\right) \cos\left(\frac{k_z}{2}\right), \quad (58)$$

where r_4 is the hopping coefficient, r_1 , r_2 and r_3 is the SOC coefficients.

The hopping terms between $(\frac{1}{2}, \frac{1}{2}, 0)$ and $(0, 0, \frac{1}{2})$ atoms are

$$H_{57} = 4 \cos\left(\frac{k_x}{2}\right) \left[(is_2 + s_6) \cos\left(\frac{k_y + k_z}{2}\right) + (-is_4 + s_8) \cos\left(\frac{k_y - k_z}{2}\right) \right], \quad (59)$$

$$H_{58} = 2 \left(\begin{aligned} & (is_3 + s_7) \cos\left[\frac{1}{2}(k_x - k_y + k_z)\right] + (-is_1 + s_5) \cos\left[\frac{1}{2}(k_x + k_y + k_z)\right] \\ & + (is_1 + s_5) \cos\left[\frac{1}{2}(k_x - k_y - k_z)\right] + (-is_3 + s_7) \cos\left[\frac{1}{2}(k_x + k_y - k_z)\right] \end{aligned} \right). \quad (60)$$

Finally, we utilize Eq. (39) to add the magnetic exchange interactions to simulate the different AFM configurations.

Although the symmetry restrictions imposed by space group operations on the anomalous Hall vector $\boldsymbol{\sigma}_H$ are the same in the three magnetic configurations, the constraints on the Néel vector \mathbf{n} differ (see Table S7). Therefore, the relations of $\boldsymbol{\sigma}_H - \mathbf{n}$ differ in different magnetic configurations. The expressions of $\boldsymbol{\sigma}_H(\mathbf{n})$ up to the third-order are:

$$\begin{cases} \boldsymbol{\sigma}_H(A) = (An_y, Bn_x, 0) + (an_x^2n_y + bn_y^3 + cn_yn_z^2, dn_x^3 + en_xn_y^2 + fn_xn_z^2, gn_xn_yn_z), \\ \boldsymbol{\sigma}_H(C) = (An_z, 0, Bn_x) + (an_x^2n_z + bn_y^2n_z + cn_z^3, dn_xn_yn_z, en_x^3 + fn_xn_y^2 + gn_xn_z^2), \\ \boldsymbol{\sigma}_H(G) = (0, An_z, Bn_y) + (an_xn_yn_z, bn_x^2n_z + cn_y^2n_z + dn_z^3, en_x^2n_y + fn_y^3 + gn_yn_z^2). \end{cases} \quad (61)$$

Table S7. Transformations of $\boldsymbol{\sigma}_H$ and \mathbf{n} in perovskite-type altermagnets with the Pnma space group. The “yes” or “no” denotes whether $\{R|\mathbf{t}\}$ switch opposite magnetic atoms or not.

Symmetry $\{R \mathbf{t}\}$	$(\sigma_x, \sigma_y, \sigma_z)$	A-type	C-type	G-type
n_a	$(\sigma_x, -\sigma_y, -\sigma_z)$	Yes $(-n_x, n_y, n_z)$	Yes $(-n_x, n_y, n_z)$	No $(n_x, -n_y, -n_z)$
m_b	$(-\sigma_x, \sigma_y, -\sigma_z)$	Yes $(n_x, -n_y, n_z)$	No $(-n_x, n_y, -n_z)$	Yes $(n_x, -n_y, n_z)$
a_c	$(-\sigma_x, -\sigma_y, \sigma_z)$	No $(-n_x, -n_y, n_z)$	Yes $(n_x, n_y, -n_z)$	Yes $(n_x, n_y, -n_z)$

Each magnetic configuration exhibits a unique $\boldsymbol{\sigma}_H - \mathbf{n}$ relationship, so our findings are significant for determining the magnetic structures of perovskite-type altermagnets. It is particularly noteworthy that if the mirror or glide mirror operations do not switch the magnetic atoms with opposite spins (as shown in Fig. S8(b)), anomalous Hall vector $\boldsymbol{\sigma}_H$ is vanished when the Néel vector \mathbf{n} is perpendicular to the mirror or glide mirror planes.

The optical Hall conductivity of A-, C-, and G-type antiferromagnetic configurations on the xoy , $yozy$, and $yozy$ planes are given in Fig. S8(c-d). The calculation results are consistent with Eq. (61), indicating that the AHE results are also suitable to the magneto-

optical effect (Kerr and Faraday effect), because the magneto-optical effect and AHE share the same symmetry requirements.

Due to the absence of higher rotational or screw symmetry, the first-order coefficients A and B are not equal or opposite in Eq. (61). Therefore, the anomalous Hall vector $\boldsymbol{\sigma}_H$ can be decomposed into Dresselhaus-like $\frac{(A+B)}{2}(n_y, n_x, 0)$ and Rashba-like $\frac{(A-B)}{2}(n_y, -n_x, 0)$ components. We found that $A \gg B$ for the A-type TB models, as shown in Fig. S8(c), forming a persistent-like AHNTs.

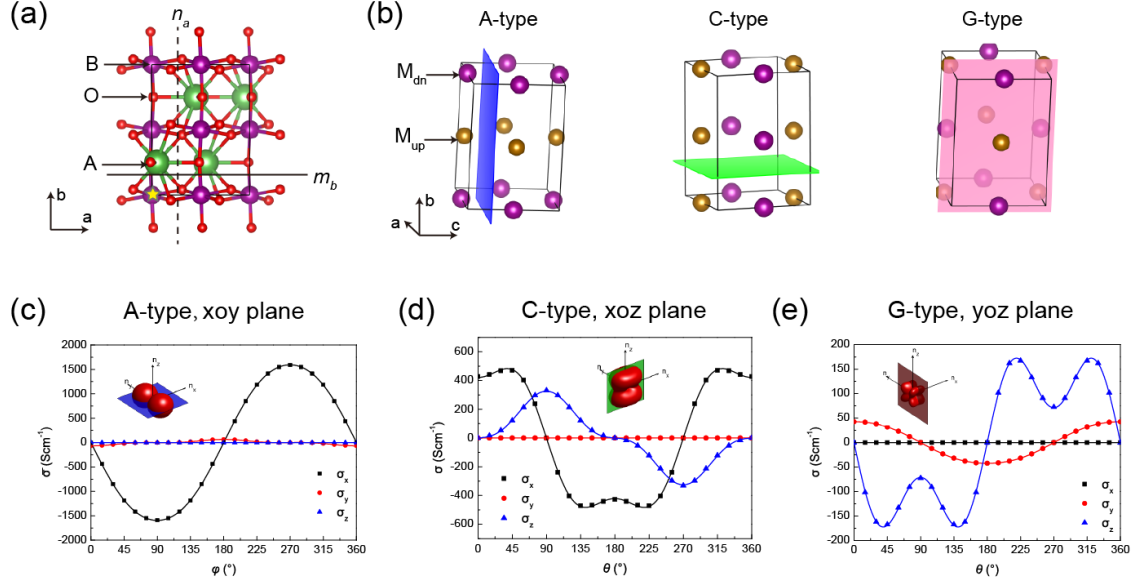


Fig. S8. (a) Crystal structure of perovskite-type altermagnetic materials ABO₃. (b) Magnetic structure of A-, C- and G-type antiferromagnetic configurations. The magnetic atoms with different spins are represented with different colors. The colored planes indicate that the mirror or glide mirror operations do not switch the magnetic atoms with opposite spins. (c, d, e) Angle dependent of $\overline{\boldsymbol{\sigma}}_H$ for A-, C-, and G-type perovskite-type altermagnetic materials, respectively. The solid lines are the fitting curves by Eq. (61). The inserts show the absolute values of $\overline{\boldsymbol{\sigma}}_H$ in the Néel vector space. Here, $\overline{\boldsymbol{\sigma}}_H = \int_{0+}^{\infty} \boldsymbol{\sigma}_H(\omega) d\omega$ [22]. $t_3=0.55$ eV, $r_4=0.54$ eV, $s_6=0.53$ eV, $s_8=0.52$ eV, $t_1=0.0497$ eV, $t_2=0.0499$ eV, $r_1=0.0501$ eV, $r_2=0.502$ eV, $r_3=0.503$ eV, $s_1=0.0501$ eV, $s_2=0.0503$ eV, $s_3=0.0505$ eV, $s_4=0.0507$ eV, $s_5=0.0509$ eV, $s_7=0.0511$ eV, $m=5.0$ eV in Eq. (52) are adopted.

The AHE in perovskite-type materials has been observed [23-26] previously. If the AHE stems from the uncompensated magnetic moments associated with magnetic atomic vacancies, it tends to exhibit a radial AHNTs with magnetic moments. With our theoretical model, however, since perovskite-type materials are altermagnetic [8-10], the intrinsic AHE usually exhibits the perpendicular $\boldsymbol{\sigma}_H \perp \mathbf{n}$ characteristics, leading to in-plane AHE. Therefore, AHNTs, explicitly linking $\boldsymbol{\sigma}_H$ and \mathbf{n} , enable us to clarify the controversy on the mechanisms of AHE in altermagnets.

Section IX. Magnetic group method for determining the anomalous Hall vector.

Since anomalous Hall vector σ_H is a pseudovector, the symmetry constraints for σ_H under the operations of R and IR are the same:

$$IR\sigma_H = R\sigma_H, \quad (62)$$

where I is the inversion operation. For an anti-unitary point operation $R' = TR$, σ_H is transformed as

$$R'\sigma_H = -R\sigma_H, \quad (63)$$

because time-reversal operation T reverses σ_H . Based on the above analysis, there are 31 magnetic point groups, including 13 original and 18 black-white magnetic point groups, possess the nonzero σ_H , which are listed in Table S8 [27].

Table S8. Symmetry-constrained anomalous Hall vector σ_H in magnetic point groups [27].

Crystallographic system	MPG	anomalous Hall vector σ_H
Triclinic	$1, \bar{1}$	$(\sigma_x, \sigma_y, \sigma_z)$
Monoclinic	Original point groups: $2, 2/m(2//y), m(m \perp y)$	$(0, \sigma_y, 0)$
	Black-White groups: $2', m', 2'/m'$	$(\sigma_x, 0, \sigma_z)$
Orthorhombic	Black-White groups: $2'2'2, m'm'2, m'm'm$	$(0, 0, \sigma_z)$
	Black-White group: $m'm2'$	$(0, \sigma_y, 0)$
Tetragonal, Trigonal, Hexagonal	Original point groups: $4, \bar{4}, 4/m, 3, \bar{3}, 6, \bar{6}, 6/m$	$(0, 0, \sigma_z)$
	Black-White groups: $42'2', 4m'm', \bar{4}2'm', 4/mm'm'$ $32', 3m', \bar{3}m', 62'2', 6m'm', \bar{6}m'2', 6/mm'm'$	

When the magnetic moments of an altermagnets are arranged along a specific direction, we can identify its magnetic space group and magnetic point group, and subsequently determine the direction of the anomalous Hall vector based on Table S8. Table S9, Table S10, and Table S11 provide detailed judgments for rutile-type, NiAs-type, and perovskite-type altermagnets. The results align with those from MTENSOR in Bilbao Crystallographic Server (<https://www.cryst.ehu.es/cgi-bin/cryst/programs/mtensor.pl>). The results align

with our “extrinsic parameter” method, and the later enables the establishment of the relationships among different magnetic orientations.

Table S9. Magnetic space groups and corresponding anomalous Hall vectors σ_H for rutile altermagnets materials with different Néel vectors.

Néel vector	Magnetic space group	σ_H
[100] (x)	Pn'nm'	(0, σ_y , 0)
[010] (y)	Pnn'm'	(σ_x , 0, 0)
[110]	Cmm'm'	(σ_x , σ_x , 0)
[001] (z)	P4 ₂ '/mnm'	0
[$a0b$] (xoz)	P2 ₁ /c.1	(0, σ_y , 0)

Table S10. Magnetic space groups and corresponding anomalous Hall vectors σ_H for NiAs-type altermagnets with different Néel vectors.

Néel vector	Magnetic space group	σ_H
[100] (x)	Cmcm.1	\times
[120] (y)	Cm'c'm	(0, 0, σ_z)
[001] (z)	P6 ₃ '/m'm'c	\times
[121]	C2'/m'	(0, σ_y , σ_z)

Table S11. Magnetic space groups and corresponding anomalous Hall vectors σ_H for perovskite-type altermagnets with different Néel vectors. The symbols in the brackets denote the nonzero anomalous Hall conductivity components.

	A-type	C-type	G-type
[100] (x)	Pn'ma' (σ_y)	Pn'm'a (σ_z)	Pnma.1 (\times)
[010] (y)	Pnm'a' (σ_x)	Pnma.1 (\times)	Pn'm'a (σ_z)
[001] (z)	Pnma.1 (\times)	Pnm'a' (σ_x)	Pn'ma' (σ_y)

It is noteworthy that the magnetic group method cannot determine the $\sigma_H - \mathbf{n}$ relation when the Néel vector is along a general direction. This is because that σ_H is the function of magnetic group in the methodology, and magnetic groups is not a good parameter. The magnetic group method encounters difficulties in addressing this issue, primarily due to treating the magnetic order parameters as intrinsic structural parameters, like crystal

structures. On the contrary, the extrinsic parameter method takes the magnetic order as an extrinsic parameter rather than an intrinsic structural parameter.

Section X. The application of AHNTs

Based on the $\sigma_H - \mathbf{n}$ relation, we can deduce the orientation of the Néel vector \mathbf{n} more conveniently, as illustrated in Fig. S9(a) because of the analytical $\sigma_H(\mathbf{n})$. Moreover, we can develop a vertical magneto-optical isolator, as depicted in Fig. S9(b). We can alter the σ_H in the horizontal direction by controlling the direction of the Néel vector in the vertical direction, thereby adjusting the magnitude of the Faraday effect and switch the of on-off light. This design may offer advantages over traditional isolators, where the magnetic field is applied along the light's path, thereby limiting the size of the magnet.

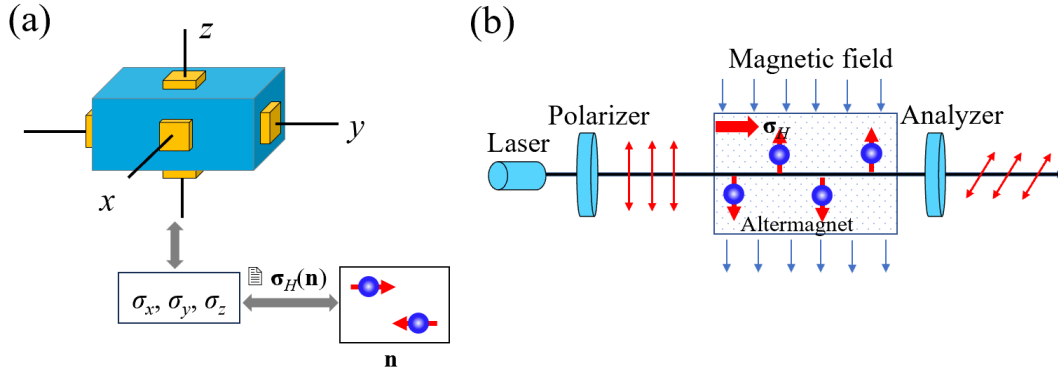


Fig. S9. (a) Schematic diagram to determine the Néel vector in an altermagnet with AHE or magneto-optical effect. σ_x , σ_y and σ_z are the anomalous Hall conductivity along the x -, y -, and z -directions, respectively. (b) A model for vertical magneto-optical isolator by utilizing the universal relationship $\sigma_H \perp \mathbf{n}$ in altermagnets.

References

- [1] W. Peng, Z. Liu, H. Pan, P. Wang, Y. Chen, J. Zhang, X. Yu, J. Shen, M. Yang, Q. Niu *et al.*, Observation of the In-plane Anomalous Hall Effect induced by Octupole in Magnetization Space, arXiv:2402.15741 (2024).
- [2] H. Pan, H. Li, J. Huang, Z. Liu, M. Fang, Y. Yuan, D. Liu, X. Hu, W. Peng, Z. Liang *et al.*, Orthogonal Geometry of Magneto-Optical Kerr Effect Enabled by Magnetization Multipole of Berry Curvature, arXiv:2412.09857 (2024).
- [3] Z. Liu, M. Wei, D. Hou, Y. Gao, and Q. Niu, Multipolar Anisotropy in Anomalous Hall Effect from Spin-Group Symmetry Breaking, arXiv:2408.08810 (2024).
- [4] S. V. Gallego, J. Etxebarria, L. Elcoro, E. S. Tasci, and J. M. Perez-Mato, Automatic calculation of symmetry-adapted tensors in magnetic and non-magnetic materials: a new tool of the Bilbao Crystallographic Server, *Acta Crystallogr. A Found Adv.* **75**, 438 (2019).
- [5] J. Železný, H. Gao, A. Manchon, F. Freimuth, Y. Mokrousov, J. Zemen, J. Mašek, J. Sinova, and T. Jungwirth, Spin-orbit torques in locally and globally noncentrosymmetric crystals: Antiferromagnets and ferromagnets, *Phys. Rev. B* **95**, 014403 (2017).
- [6] L. L. Tao and E. Y. Tsybal, Perspectives of spin-textured ferroelectrics, *J. Phys. D: Appl. Phys.* **54**, 113001 (2021).

- [7] C. Mera Acosta, L. Yuan, G. M. Dalpian, and A. Zunger, Different shapes of spin textures as a journey through the Brillouin zone, *Phys. Rev. B* **104**, 104408 (2021).
- [8] L. Šmejkal, J. Sinova, and T. Jungwirth, Beyond Conventional Ferromagnetism and Antiferromagnetism: A Phase with Nonrelativistic Spin and Crystal Rotation Symmetry, *Phys. Rev. X* **12**, 031042 (2022).
- [9] L. Šmejkal, J. Sinova, and T. Jungwirth, Emerging Research Landscape of Altermagnetism, *Phys. Rev. X* **12**, 040501 (2022).
- [10] Y. Guo, H. Liu, O. Janson, I. C. Fulga, J. van den Brink, and J. I. Facio, Spin-split collinear antiferromagnets: A large-scale ab-initio study, *Matter. Today Phys.* **32**, 100991 (2023).
- [11] Xiaobing Chen, Yuntian Liu, Pengfei Liu, Yutong Yu, J. L. Jun Ren, Ao Zhang, and Q. Liu, Catalog of Unconventional Magnons in Collinear Magnets, [arXiv:2307.12366](https://arxiv.org/abs/2307.12366) (2023).
- [12] I. Sodemann and L. Fu, Quantum Nonlinear Hall Effect Induced by Berry Curvature Dipole in Time-Reversal Invariant Materials, *Phys. Rev. Lett.* **115**, 216806 (2015).
- [13] R.-C. Xiao, D.-F. Shao, W. Huang, and H. Jiang, Electrical detection of ferroelectriclike metals through the nonlinear Hall effect, *Phys. Rev. B* **102**, 024109 (2020).
- [14] Z. Z. Du, H.-Z. Lu, and X. C. Xie, Nonlinear Hall effects, *Nat. Rev. Phys.* **3**, 744 (2021).
- [15] M. T. Suzuki, T. Koretsune, M. Ochi, and R. Arita, Cluster multipole theory for anomalous Hall effect in antiferromagnets, *Phys. Rev. B* **95**, 094406 (2017).
- [16] M. Yatsushiro, H. Kusunose, and S. Hayami, Multipole classification in 122 magnetic point groups for unified understanding of multiferroic responses and transport phenomena, *Phys. Rev. B* **104**, 054412 (2021).
- [17] S. Bhowal and N. A. Spaldin, Ferroically Ordered Magnetic Octupoles in d-Wave Altermagnets, *Phys. Rev. X* **14**, 011019 (2024).
- [18] Z. Zhang, Z.-M. Yu, G.-B. Liu, and Y. Yao, MagneticTB: A package for tight-binding model of magnetic and non-magnetic materials, *Comput. Phys. Commun.* **270**, 108153 (2022).
- [19] L. Šmejkal, R. González-Hernández, T. Jungwirth, and J. Sinova, Crystal time-reversal symmetry breaking and spontaneous Hall effect in collinear antiferromagnets, *Sci. Adv.* **6**, eaaz8809 (2020).
- [20] M. e. Roig, A. Kreisel, Y. Yu, B. M. Andersen, and D. F. Agterberg, Minimal Models for Altermagnetism, [arXiv:2402.15616](https://arxiv.org/abs/2402.15616) (2024).
- [21] T. P. T. Nguyen and K. Yamauchi, Ab initio prediction of anomalous Hall effect in antiferromagnetic CaCrO_3 , *Phys. Rev. B* **107**, 155126 (2023).
- [22] X. Zhou, W. Feng, X. Yang, G.-Y. Guo, and Y. Yao, Crystal chirality magneto-optical effects in collinear antiferromagnets, *Phys. Rev. B* **104**, 024401 (2021).
- [23] D. J. Wang, J. R. Sun, S. Y. Zhang, G. J. Liu, B. G. Shen, H. F. Tian, and J. Q. Li, Hall effect in $\text{La}_{0.7}\text{Ce}_{0.3}\text{MnO}_{3+\delta}$ films with variable oxygen content, *Phys. Rev. B* **73**, 144403 (2006).
- [24] K. Li, R. Cheng, Z. Chen, J. Fang, X. Cao, and Y. Zhang, Anomalous Hall conductivity and magnetoresistance in epitaxial $\text{La}_{0.67}\text{Ca}_{0.33}\text{MnO}_{3-\delta}$ thin films, *J. Appl. Phys.* **84**, 1467 (1998).
- [25] T. Asaba, Z. Xiang, T. H. Kim, M. S. Rzchowski, C. B. Eom, and L. Li, Unconventional ferromagnetism in epitaxial (111) LaNiO_3 , *Phys. Rev. B* **98**, 121105 (2018).
- [26] M.-W. Yoo, J. Tornos, A. Sander, L.-F. Lin, N. Mohanta, A. Peralta, D. Sanchez-Manzano, F. Gallego, D. Haskel, J. W. Freeland *et al.*, Large intrinsic anomalous Hall effect in SrIrO_3 induced by magnetic proximity effect, *Nat. Commun.* **12**, 3283 (2021).
- [27] R.-C. Xiao, D.-F. Shao, W. Gan, H.-W. Wang, H. Han, Z. G. Sheng, C. Zhang, H. Jiang, and H. Li, Classification of second harmonic generation effect in magnetically ordered materials, *npj Quantum Mater.* **8**, 62 (2023).